A Scalable THz Photonic Crystal Fiber With Partially-Slotted Core That Exhibits Improved Birefringence and Reduced Loss

Tianyu Yang, Can Ding, *Member, IEEE*, Richard W. Ziolkowski, *Fellow, IEEE, Fellow, OSA*, and Y. Jay Guo, *Fellow, IEEE*

***Abstract*—A photonic crystal fiber (PCF) based on high resistivity silicon is reported that exhibits high birefringence, low loss, and flat dispersion characteristics across a wide bandwidth in the THz regime. Except for the center region, which remains the background dielectric, its core is occupied by a set of rectangular air slots. The material and configuration lead to high birefringence and low loss. The simulation results, which include the material losses, indicate that a birefringence value of 0.82 and a total loss of 0.011 cm^{-1}, including the effective material loss and confinement losses, are achieved at 1.0 THz. These values are a factor of ten times higher and four times lower, respectively, than many recent designs. The numerical analyses also demonstrate that the reported PCF can be scaled to any desired portion of the THz regime, while maintaining a similar birefringence, simply by changing the lattice constant. This "scalable" characteristic is shown to be applicable to other PCF designs. It could facilitate a novel way of testing THz fibers, i.e., it suggests that one only needs to test the preform to validate the performance of the fiber at higher frequencies. This outcome would significantly reduce the design complexity and the costs of PCF testing.**

***Index Terms*—Birefringence, confinement loss (CL), dispersion, effective material loss (EML), photonic crystal fiber (PCF), terahertz.**

I. Introduction

BECAUSE wireless technologies have been enhancing many aspects of people's life, the demand for access to data has dramatically increased over the last few years. It is reported that the data rates have doubled every eighteen months over the last three decades and are approaching the capacity limit of current wireless communication systems [1]. To meet the expected continuation of this growth, terahertz (THz) band communications are envisioned as the next frontier of wireless communications [2]. The THz band, which covers the spectral range from 0.1 THz to 10 THz, could effectively alleviate the spectrum scarcity and capacity limitations of current systems. While both frequency regions below (microwave) and above (optical) this band have been extensively investigated, many features of THz technology are only now being studied.

Arrays of millimeter-wave and THz sources could deliver the highly directive beams desired for these next generation systems. However, because of large losses, the propagation of THz waves in many user environments remains a significant challenge. Several approaches may yield practical guided wave solutions to realize the feed networks associated with THz arrays. One is the open air, quasi-optical transmission method [3]. It is not an effective approach because the waves are not shielded and may couple with other devices in the communication system. Substrate integrated waveguides and metallic waveguides are traditional millimeter-wave solutions. However, they also suffer from unacceptable losses in the THz regime. Feed networks based on graphene [4] are also a possible and have attracted recent attention. Nonetheless, their current fabrication difficulties and high costs remain as severe obstacles to their practical application. Stainless solid wires [5], metal-coated dielectric tubes [6], and hypodermic needles [7] can also act to guide THz waves, but they also suffer from high propagation losses.

In contrast, optical fiber-based wave guiding systems serve as promising candidates for the short range THz wave guiding needed to advance THz communication systems. For instance, signals can be suitably confined inside the fiber, thus avoiding unwanted coupling with other devices. Moreover, fibers are flexible and can be adapted to a variety of packaging requirements. Furthermore, fiber drawing techniques are mature technologies in the optical regime and could lead to easier fabrication and experiment verification of THz components. Many polymer fibers, including plastic fibers [8], Bragg fibers [9], and photonic crystal fibers (PCFs) [10], have been reported recently for THz applications.

Among these different fiber types, the PCFs are very suitable for short range THz applications. They exhibit low losses while having structural flexibility. Typical optical PCFs utilize a solid dielectric as the fiber core and insert air holes to form its cladding [11]. This structure generates the necessary index differences between the cladding and the core to promote the desired wave guiding. Recent advances in THz PCFs have

Manuscript received March 22, 2018; revised May 25, 2018; accepted May 28, 2018. This work was supported by Australian Research Council under Grant DP160102219. *(Corresponding author: Can Ding.)*

T. Yang, C. Ding, and Y. J. Guo are with the Global Big Data Technologies Centre, University of Technology Sydney, Ultimo, NSW 2007, Australia (e-mail: tianyu.yang@student.uts.edu.au; can.ding.1989@gmail.com; Jay.Guo@uts.edu.au).

R. W. Ziolkowski is with the Global Big Data Technologies Centre, University of Technology Sydney, Ultimo, NSW 2007, Australia, and also with the Department of Electrical and Computer Engineering, The University of Arizona, Tucson, AZ 85721 USA (e-mail: ziolkows@email.arizona.edu).

Color versions of one or more of the figures in this paper are available online at http://ieeexplore.ieee.org.

Digital Object Identifier 10.1109/JLT.2018.2842825

included the introduction of additional smaller air holes in the core area [12]–[14]. The aim of these porous fiber designs is to trap the majority of the wave energy in the air regions to minimize the propagation loss.

When designing THz wave guides, the most stressed factors are their loss properties, i.e., their effective material loss (EML) and confinement loss (CL). While there are other loss mechanisms, e.g., bending and scattering losses, the EML and CL losses represent the major ones in THz PCFs and are the benchmarks of this work. Many recent PCF studies have focused on achieving a low EML. An octagonal porous PCF was proposed in [14]; it was shown to have a low EML, 0.07 cm^{-1}, at a 1.0 THz operating frequency. However, the CL was not considered. Another design [15] achieved an ultra-low EML of 0.056 cm^{-1} and a CL of 0.03 cm^{-1} at 1.0 THz. A PCF employing a rotated porous hexagonal core [16] was designed to have an EML of 0.066 cm^{-1} and a CL of 4.73×10^{-4} cm^{-1} at 1.0 THz [16]. An even lower EML and CL values were realized theoretically in [17], but under an extreme assumption that cannot be realized in practice. The loss values in [18] are generally the state-of-art for THz PCFs, but that PCF was targeted for long range applications and may not be suitable for short range ones.

For short range signal transmissions, PCFs are also required to have a high birefringence in order to maintain polarization integrity over a short distance [19]. This guided wave feature is widely introduced by breaking the symmetry of either the core area or the holey cladding. For example, a rectangular porous fiber with a birefringence of 0.012 at 0.65 THz has been achieved experimentally [12]. The birefringence was realized by introducing rectangular slots into the core area. This PCF exhibited a reasonable EML below 0.25 cm^{-1} for frequencies below 0.8 THz. Similarly, squeezed elliptical holes were etched into the PCF core area in [20], achieving a birefringence on the order of 10^{-2}. An asymmetric distribution of circular air-holes was utilized in both the cladding and the core area of a PCF in [10] to achieve a high birefringence of 0.026. Introducing a single circular air-hole unit into the core area, an oligo porous-core PCF has been realized with a high birefringence of 0.03 [21]. A new kind of dual-hole unit-based porous-core hexagonal PCF was presented in [22] that yielded a low EML $= 0.1$ cm^{-1}, a low CL $= 10^{-3}$ cm^{-1}, and a high birefringence $=0.033$ at an operating frequency of 0.85 THz. A circular air hole PCF with asymmetries both in the core and the cladding was proposed in [23] and yielded an even higher birefringence $=0.045$ and a lower EML $= 0.08$ cm^{-1}. Other works based on slot cladding, circular lattice cladding, and kagome cladding were presented in [24]–[26] that also exhibited reasonable birefringence and loss values.

While most of these published works focused on a narrow band of frequencies around 1.0 THz, wide bandwidth fibers are preferred for high data capacity realizations. Consequently, another key performance factor that must be considered is dispersion. A rapidly-changing dispersion results in a significant performance variation across the bandwidth and, thus, should be avoided. Consequently, high birefringence, low loss, and flat dispersion in a wide bandwidth are all highly desirable design goals for THz fiber-based components. These often conflicting properties make achieving them all simultaneously a very challenging problem.

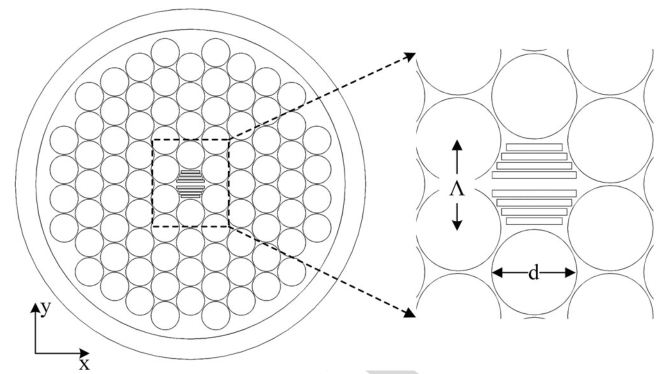

Fig. 1. Cross sectional view of the reported PCF.

A THz PCF with a partially-slotted core based on high resistivity silicon (HRS) [27] is presented in this paper. It is able to simultaneously achieve high birefringence, low loss, and flat dispersion over a broad band of frequencies. Rectangular slots are inserted into the fiber core. These air holes destroy the symmetry of the core. Nonetheless, the center area of the core remains a solid dielectric. The birefringence and loss performance can be noticeably improved with this configuration. Parameter sweeps of the key dimensions are presented to illustrate how the design is tuned to have the best performance characteristics. Numerical analyses will demonstrate that the reported PCF has a high birefringence, above 0.76, and a low total loss, below 0.04 cm^{-1} for both polarizations over a broad range from 0.9 to 1.3 THz. The dispersion variations for the two orthogonal polarized states are 0.6 ps/THz/cm and 0.5 ps/THz/cm from 0.8 to 1.1 THz, respectively. Comparisons with an analogous design based on the popular material Topas [28] further illustrate the significant advantages of the choice of HRS. Moreover, silicon has been used successfully in a variety of fiber and THz waveguide works [29]–[32].

Another contribution reported in this paper is the recognition of a "scaling property" of PCFs. In particular, by properly scaling all of the dimensions of the reported PCF, the working frequency can be shifted while maintaining its birefringence and loss properties. It is demonstrated that this scaling is generally true for different materials across a broad band of frequencies where the background material shows near zero dispersion. Additionally, another published PCF design [22] is used to illustrate that this scaling principle is universal as long as the material dispersion is near zero. Furthermore, it suggests an easier means to test PCFs in the THz regime. By only testing the preform, the performance of the PCF can be obtained without drawing it into the final fiber. This outcome would significantly reduce the cost of the development and testing of THz PCFs.

II. PCF Configuration

Fig. 1 shows the cross section of the partially-slotted (PS) PCF based on HRS. A triangular lattice distribution of five air-hole rings is used as the cladding. The distance between adjacent air holes is the lattice constant Λ. The diameter of the circular air holes in the cladding is set equal to $d = 0.95\ \Lambda$. Outside of the cladding, a matching layer is employed whose thickness is 15% of the whole diameter of the PCF. There are eight rectangular slot-shaped air holes distributed symmetrically with respect to the *x*-axis in the core area. The center of the core is solid, the background dielectric. The remainder of the core is partially slotted. The lengths L of each slot in each set of four are 0.957 Λ, 0.851 Λ, 0.745 Λ, and 0.638 Λ, respectively, from its middle to its edge. The width of all of the slots is W = 0.04 Λ and the distance between any two adjacent slots is D = 0.105 Λ. The dielectric in the core center has a fixed width of 0.132 Λ. Note that all the dimensions have been described in terms of the lattice constant Λ. This choice is an optimal way to describe the PCF; it facilitates the scaling property that will be introduced below. The optimized lattice constant value was found to be $\Lambda = 100\ \mu$m.

As noted, both HRS [27] and Topas [28] were considered as the background dielectric material. On one hand, we have found that HRS, whose material absorption loss is less than 0.015 cm^{-1} below 1.5 THz and whose refractive index n = 3.417 from 0.5 to 4.5 THz, leads to superior birefringence and loss properties across a wider band. On the other hand, a number of PCF studies have used Topas because of its low bulk material absorption loss <0.2 cm^{-1} and stable refractive index n = 1.5258 below 1.0 THz. Since the refractive indexes of these two materials are different, the Topas-based PCF parameters must be obtained separately. It was found that the same PS design was optimized with Topas simply by setting $\Lambda = 400\ \mu$m and W = 0.078 Λ.

III. Numerical Simulations

The simulations in this work were conducted with the commercial software COMSOL Multiphysics. It is based on the full-vector finite element method (FEM). Perfectly matched layer (PML) boundary conditions were employed.

To demonstrate the superiority of the PS configuration over the commonly known fully-slotted (FS) configuration [24]–[26], simulations were performed for both HRS-based and Topas-based PCFs with and without the center slot. For these comparison PCF designs to be commensurate with published works, the lattice constant Λ was set to be 100 μm.

The HRS-based FS PCF is attained simply by adding a slot with the optimized dimensions: $L \times W = 1.064\ \Lambda \times 0.04\ \Lambda$ to the corresponding FS design. The electric field distributions in the central regions of the HRS-based PS and FS PCFs are presented in Fig. 2 for both the X-polarized (X-pol) and Y-polarized (Y-pol) modes. As illustrated, the differences between the HRS-based PS and FS PCFs are not significant. This is simply due to the fact that the slot is quite narrow. Nevertheless, quantitative comparisons based on the birefringence and loss values given below demonstrate that the PS configuration is superior to the FS one. On the other hand, it is clear that the X-pol fields are more strongly confined to the core than the Y-pol ones. In fact, more than two to three times the power is localized in the core for the X-pol mode in comparison to the Y-pol mode over the frequencies of interest.

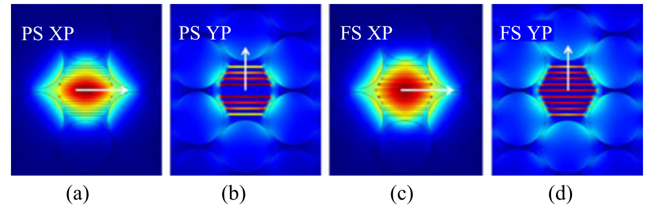

Fig. 2. The magnitude of the electric field distributions at 1.0 THz for the HRS-based PCFs. (a) X- and (b) Y-pol modes of the PS PCF. (c) X- and (d) Y-pol modes of the FS PCF. (The arrows represent the direction of the electric field vector. The color spectrum for each subplot represents the same power levels (dark red is maximum; dark blue is minimum).)

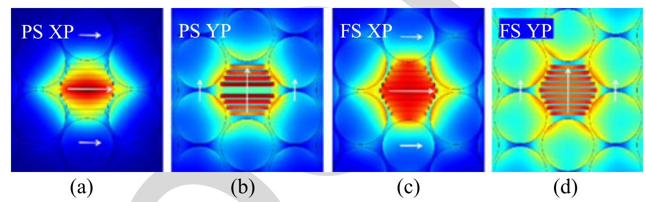

Fig. 3. The magnitude of the electric field distribution at 1.0 THz for the Topas-based PCFs. (a) X- and (b) Y-pol modes of the PS PCF. (c) X- and (d) Y-pol modes of the FS PCF. (The arrows represent the direction of the electric field vector. The color spectrum for each subplot represents the same power levels (dark red is maximum; dark blue is minimum).)

Similarly, the central slot for the Topas-based FS PCF has the optimized dimensions: $L \times W = 1.064\ \Lambda \times 0.078\ \Lambda$. The electric field distributions in the central regions of both the PS and FS designs are presented in Fig. 3. The X- and Y-pol modes of the FS PCF presented in Fig. 3(c) and (d) clearly show that more power is distributed in its cladding when compared to the same modes for the PS PCF shown in Fig. 3(a) and (b). Similarly, it is also clear that more power is present in the central region of the PS design.

These large differences in the behaviors of the PS and FS Topas designs arise from their wider slots and their lower substrate index contrast. These features lead to an effective index of the core region which is relatively low and, hence, poorer confinement there. Nonetheless, the higher percentage of the dielectric remaining in the core of both the HRS- and Topas-based PS structures improves the index contrast between it and the cladding. This leads to improved field confinement in the PS cores. Consequently, a much higher birefringence is attained, for example, with the Topas-based PS PCF (0.069) in comparison to the FS PCF (0.025) at 1 THz.

As is also observed in Fig. 3, the electric field of the X-pol mode is strongly concentrated in the core. In contrast, a noticeable proportion of the electric field appears in the cladding for the Y-pol mode. Moreover, the electric field of the Y-pol mode remains mainly in the air slots; very little is distributed into the dielectric. On the other hand, the X-pol electric field has no apparent preferences between the air slots or dielectric in the core region.

The key performance indexes of the HRS-based PS and FS PCFs: the CL, EML, birefringence, and dispersion values, are compared in Fig. 4 as functions of the source frequency. Following [18], the CL values shown in Fig. 4(a) were

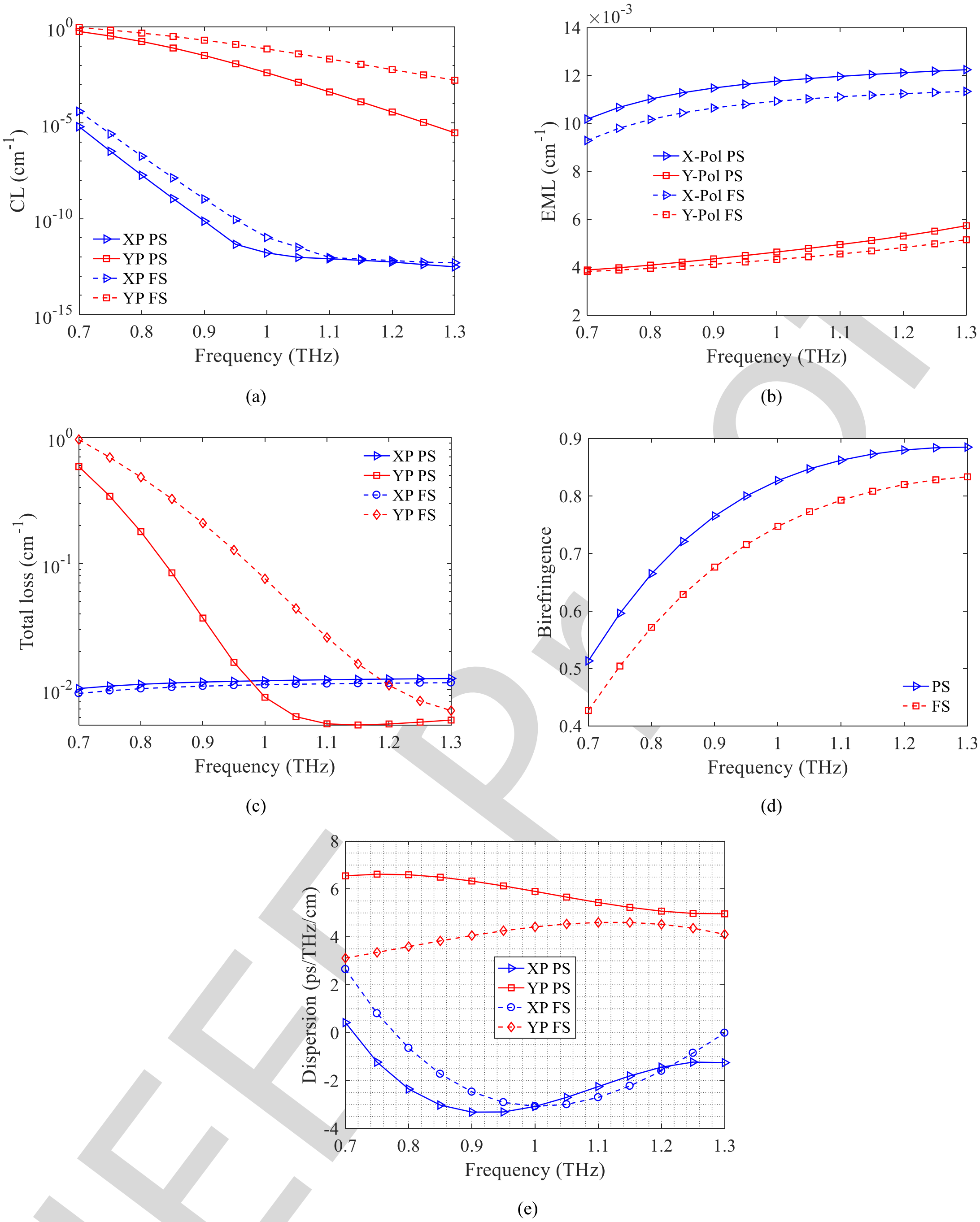

Fig. 4. Comparison of the simulated performance characteristics of the X- and Y-pol modes of the HRS-based PS (solid lines) and FS (dashed lines) PCFs. The (a) CL, (b) EML, (c) total loss, (d) birefringence, and (e) dispersion values as functions of the source frequency. (Note: XP denotes X-pol; YP denotes Y-pol.)

calculated as

$$L_c\left(\mathrm{cm}^{-1}\right) = \frac{4\pi f}{c} \times Im\ [n_{\mathrm{eff}}], \quad (1)$$

where c is the speed of light in vacuum and $\mathrm{Im}[n_{\mathrm{eff}}]$ is the imaginary part of the effective refractive index. As observed in Fig. 4(a), the CL values for both the X- and Y-pol modes are smaller in the PS PCF. Furthermore, the X-pol CL values are observed to be significantly smaller than the Y-pol ones for both the PS and FS PCFs.

The reason that the CL values in the X-pol modes are significantly lower than the Y-pol modes arises from the much stronger confinement in the core in the former and the presence of the air-filled slots in the core. One finds that about half the X-pol power in the core is associated with the slot regions which are filled with air. This is actually discernable in Fig. 2(a) and (b). Consequently, the values of $\mathrm{Im}[n_{\mathrm{eff}}]$ are tiny. While Fig. 2(b) and (d) show the fields in the slots are much larger than their surrounding dielectric, they also illustrate the much poorer confinement in the core. Thus, while the Y-pol values of $\mathrm{Im}[n_{\mathrm{eff}}]$ are relatively small, they are not tiny. Moreover, because of the nature of the Y-pol band-gap structure formed by the slots, the defect region in the PS structure (i.e., the HRS center of the core) causes the fields outside of the core to be lower than those in the FS structure. This smaller confinement thus causes the Y-pol Im$[n_{\mathrm{eff}}]$ values to be larger in the FS case. The slightly different X-pol CL values for the PS and FS structures arise from the slightly poorer confinement observed between Fig. 2(a) and (c).

The EMLs of both modes and PCFs are plotted in Fig. 4(b). They were obtained with the expression

$$\alpha_{\mathrm{eff}}\left(\mathrm{cm}^{-1}\right) = \frac{\left(\frac{\varepsilon_0}{\mu_0}\right)^{\frac{1}{2}} \int_{\mathrm{mat}} n_{\mathrm{mat}}\, \alpha_{\mathrm{mat}}\, |E|^2\, dA}{2 \int_{All} S_z\, dA}, \quad (2)$$

where ε_0 and μ_0 are the permittivity and permeability of vacuum, n_{mat} is the refractive index of the background material, α_{mat} is the bulk material absorption loss, E is the modal electric field, and S_z is the Poynting vector projection in the Z direction. As shown in Fig. 4(b), the EML values of the PS PCF are slightly higher than those of the FS design for both the two polarized modes. This outcome is simply due to the fact that the PS PCF has a slightly larger fraction of the dielectric in the core area. It also is observed that the X-pol EMLs are larger than the Y-pol EMLs. This behavior is due to the fact that the Y-pol electric field is concentrated mainly in the air slots (see Fig. 2).

Although the EML values are slightly higher for PS PCF, its CL values are lower. The total losses, considering both the EML and CL values, are presented in Fig. 4(c). These results demonstrate that the PS PCF has a much smaller loss for the Y-pol mode and a comparable loss for the X-pol mode when compared to those of the FS PCF. Because the total loss is the combination of the CL and EML values, we will only report the total loss for the parameter studies below.

The birefringence, *B*, is calculated as

$$B = |n_x - n_y|, \quad (3)$$

where n_x and n_y are the effective modal refractive indexes for the X- and Y-pol modes, respectively. The simulated birefringence values for both PCFs are given in Fig. 4(d). It is noted immediately that the birefringence of both the PS and FS PCFs is very high. Moreover, there is an enhancement of the birefringence achieved by introducing the PS core. Specifically, the birefringence is improved from 0.42 to 0.51 and from 0.83 to 0.88 at 0.7 THz and 1.3 THz, respectively. The real parts of the indexes completely dominate the birefringence calculation (3). The presence of the HRS dielectric in the center of the core of the PS structure causes the value of Re(n_{eff}) in the X-pol case to be larger than it is in the FS structure.

Fig. 4(e) shows the dispersion curves versus frequency for both PCFs and their X- and Y-pol modes. Since the material dispersion of the HRS is negligible within the 0.5–4.5 THz frequency band, these curves basically represent the effects of waveguide dispersion. The latter is calculated with the expression [18]:

$$\beta_2 = \frac{2}{c}\frac{dn_{\mathrm{eff}}}{d\omega} + \frac{\omega}{c}\frac{d^2 n_{\mathrm{eff}}}{d\omega} \quad (4)$$

where n_{eff} is specifically the effective refractive index of the fundamental mode and $\omega = 2\pi f$ is its angular center frequency. It can be seen that the dispersion curve of the PS PCF is much flatter across the frequencies of interest in comparison to the FS PCF one. In particular, the variations of the dispersion curve for both polarization states of the PS PCF are low: -2.8 ± 0.6 ps/THz/cm for the X-pol mode and 6.0 ± 0.5 ps/THz/cm for the Y-pol mode from 0.8 to 1.1 THz. It is found that the values of Re(n_{eff}) for the X-pol mode for both the PS and FS structures are larger for than those of the Y-pol mode. The slopes of the X-pol values for both structures are decreasing with increasing frequency. The slopes of the Y-pol values are positive with increasing frequency. On the other hand, the values of Im(n_{eff}) are decreasing with frequency for both modes and both structures, but they are more than two orders of magnitude smaller than the real values. These features of the effective index values lead to the exhibited negative dispersion values for the X-pol case and the positive ones for the Y-pol case.

In summary, all of these performance characteristic results clearly demonstrate the superiority of the PS configuration.

IV. Parameter Studies

Parameter sweeps were conducted to optimize the HRS-based PS PCF design. Various compromises between the different performance indexes allow one to meet different specifications. A summary of the main design parameter results provide guidelines for configuring this PCF for any of its many potential applications.

A. *Effects of the Lattice Constant* Λ

The most important design parameter is the lattice constant, Λ, particularly since all of the PCF dimensions are defined proportional to it. The simulated total loss, birefringence, and dispersion values for different Λ values are plotted in Fig. 5(a) to (c), respectively. As shown in Fig. 5(a), the total loss for the Y-pol mode decreases rapidly with an increase of lattice constant Λ. For this mode, the loss is dominated by the CL values, which are more sensitive to the dimensions of the structure. On the other hand, the total loss of the X-pol mode remains basically constant. The latter occurs because its loss is dominated by the EML, and the HRS loss value varies little across the frequencies of interest.

Fig. 5(b) illustrates the changes in the birefringence values. They increase as both the lattice constant Λ and the operating frequency increase. As Fig. 5(c) illustrates, the dispersion values for the different Λ values can exhibit rather large variations if the lattice constant is not chosen properly.

An appropriate compromise amongst all of the performance characteristic values is obtained by selecting $\Lambda = 100\ \mu$m. This HRS-based PS PCF has low losses, i.e., below 0.04 cm^{-1}, for both polarizations from 0.9 to 1.3 THz. It has birefringence values above 0.76 across this frequency range. On the other hand, its dispersion values for the less-confined X-pol mode are -2.3 ± 1.0 (43%), while they are 5.7 ± 0.7, i.e., only a 12% variation for the more-confined Y-pol mode across the same frequency range.

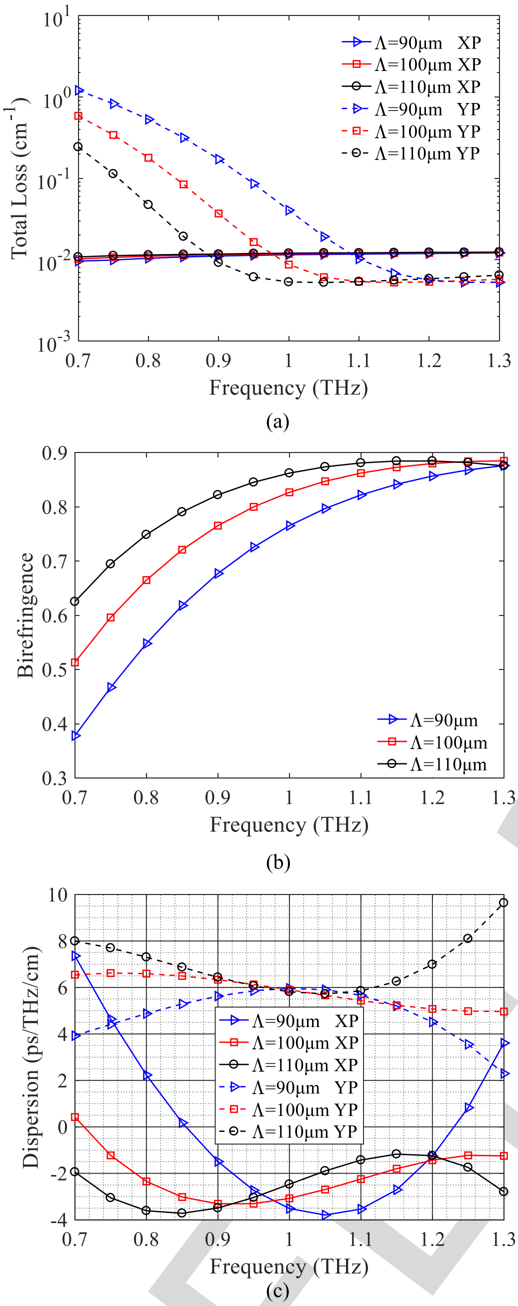

Fig. 5. Simulated (a) total loss, (b) birefringence, and (c) dispersion values of the PS PCF across a wide frequency range for different Λ values.

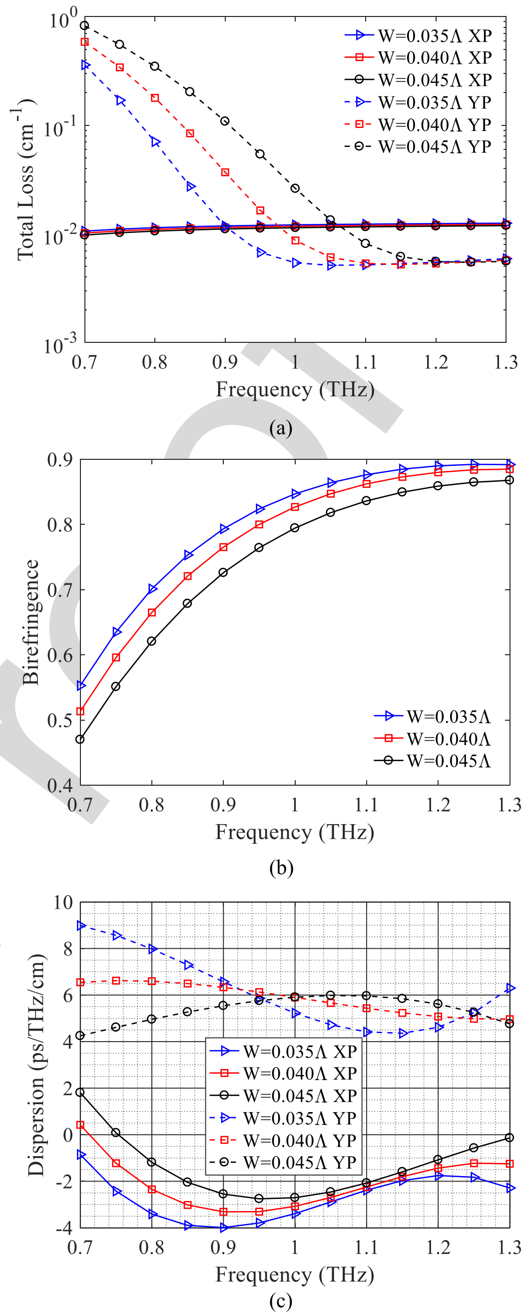

Fig. 6. Simulated (a) total loss, (b) birefringence, and (c) dispersion values of the PS PCF with $\Lambda = 100$ μm for different W across a wide frequency range.

B. Effects of the Slot Width

The slot width, W, also has a significant influence on the performance characteristics. A parameter sweep of W was conducted with all of the other dimensions remaining fixed, notably with $\Lambda = 100$ μm. The resulting variations of total loss, birefringence, and dispersion are presented in Fig. 6(a) to (c), respectively.

As observed in Fig. 6(a), the TL values are essentially constant for the X-pol modes. Because the fields are strongly confined to the core region, there is little TL variation encountered as the slot size increases. On the other hand, more loss is incurred for the Y-pol mode at lower frequencies for larger W because the fields in the HRS become larger as the edges of the slots are closer together and more strongly coupled. As the frequency increases and, hence, the wavelength decreases, this coupling decreases and the TL values decrease. The TL values eventually saturate at some higher frequency as this coupling becomes minor.

Fig. 6(b) demonstrates that the birefringence increases as W decreases and the frequency increases. This effect again arises because a higher real part of the effective n_x is realized when more HRS present for the smaller W values and a higher contrast between the core and the cladding occurs for smaller wavelengths. Fig. 6(c) indicates that the dispersion values for the

TABLE I
PERFORMANCE COMPARISONS BETWEEN THE STATES-OF-ART PCFS AND THE PCF REPORTED IN THIS WORK

Works	Confinement loss(cm^{-1})	EML (cm^{-1})	Total loss (cm^{-1})	Birefringence	Dispersion variation (ps/THz/cm)
[14]	-	0.07	-	-	-
[15]	0.03	0.057	0.087	-	0.18
[16]	$10^{-3.5}$	0.066	0.067	-	0.3
[18]	0.0012	0.035	0.036	-	0.09
[24]	0.008	0.07	0.078	0.075	0.5
[22]	10^{-3}	0.1	0.11	0.033	-
[23]	-	0.08	-	0.045	0.5
[21]	3.5	0.1	3.51	0.03	0.3
[17]	$10^{-3.7}$	0.034	0.035	0.001	0.09
[26]	10^{-9}	0.05	0.05	0.086	0.07
Topas PS YP	10^{-6}	0.071	0.071	0.069	0.07
Topas PS XP	10^{-12}	0.11	0.11		0.06
HRS PS YP	0.0041	0.0046	0.0087	0.82	0.5
HRS PS XP	10^{-12}	0.011	0.011		0.6

X-pol mode experience only minor variations for different W values, but experience larger ones for the Y-pol mode.

Consequently, we elected to set W = 0.04 Λ (4.0 μm) as the optimized value. It produces high birefringence and low loss around 1.0 THz and has the smallest variations in the dispersion values.

Finally, we note that the diameter of the circular air hole, d, also has a direct impact on the performance characteristics. A larger d yields a better confinement of the field, which in turn leads to higher birefringence and lower loss values. Nevertheless, the fabrication of the PCF is more difficult when the difference between d and Λ becomes smaller. Therefore, d was chosen to be 0.95 Λ for the optimized design as a tradeoff between of the performance values and the anticipated fabrication complexity.

C. Performance Comparison

As a final comparison between the HRS- and Topas-based PS PCFs, Fig. 7(a) and (b) present their simulated total loss and birefringence values for their optimized designs, respectively. It is noted that the Y-pol loss of the HRS-based PS PCF is quite high at the lowest frequencies, but achieves much lower loss for both two polarizations when the frequency is above 0.9 THz. On the other hand, Fig. 7(b) demonstrates conclusively that the birefringence values achieved by the HRS-based PS PCF are an order of magnitude higher than those of the corresponding Topas-based design.

In summary, the optimized HRS-based PS PCF performance characteristics are compared with the reported state-of-art PCFs as listed in Table I. Our design has the smallest loss, being nearly 4 times lower than the other designs. The birefringence achieved is remarkably ∼10 times higher than all of the reported designs.

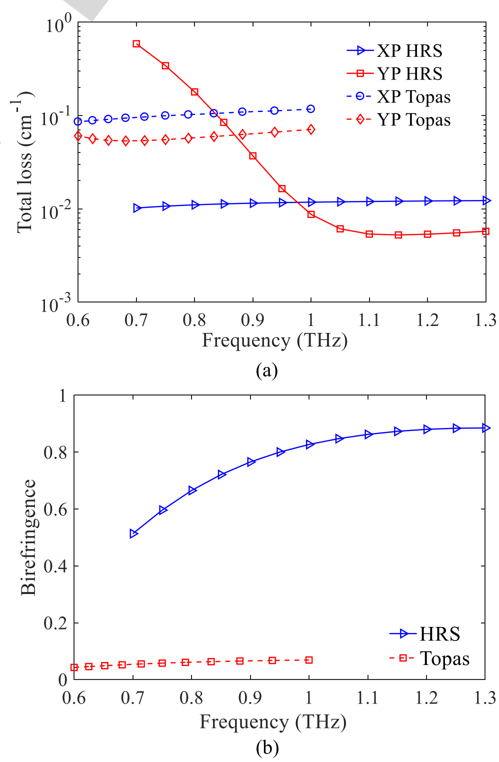

Fig. 7. Comparison of the simulated (a) total loss and (b) birefringence values of the optimized HRS- and TOPAS-based PS PCFs as functions of the source frequency.

On the other hand, the variation of the dispersion values is comparable. Furthermore, our design also provides these superior properties over a wide bandwidth rather than being limited to operation in a narrow band of frequencies around 1.0 THz.

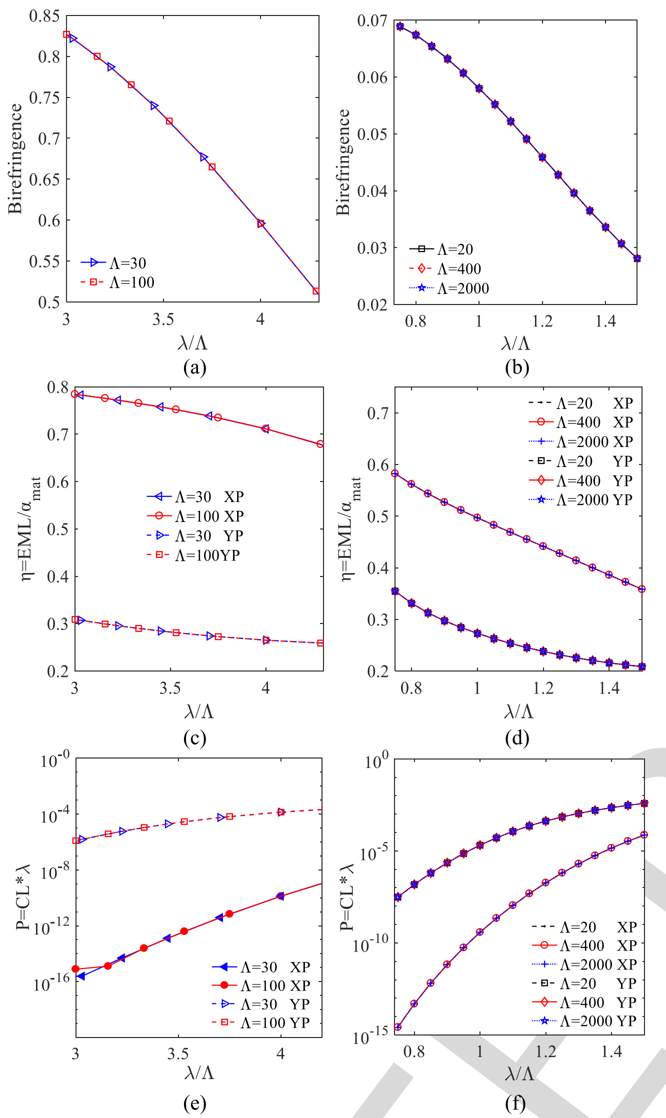

Fig. 8. Simulated (a), (b) birefringence, (c), (d) normalized EML, and (e), (f) normalized CL values across THz regime as the size of the HRS and Topas PCFs are scaled respectively. (Note that the units of Λ are micrometers.)

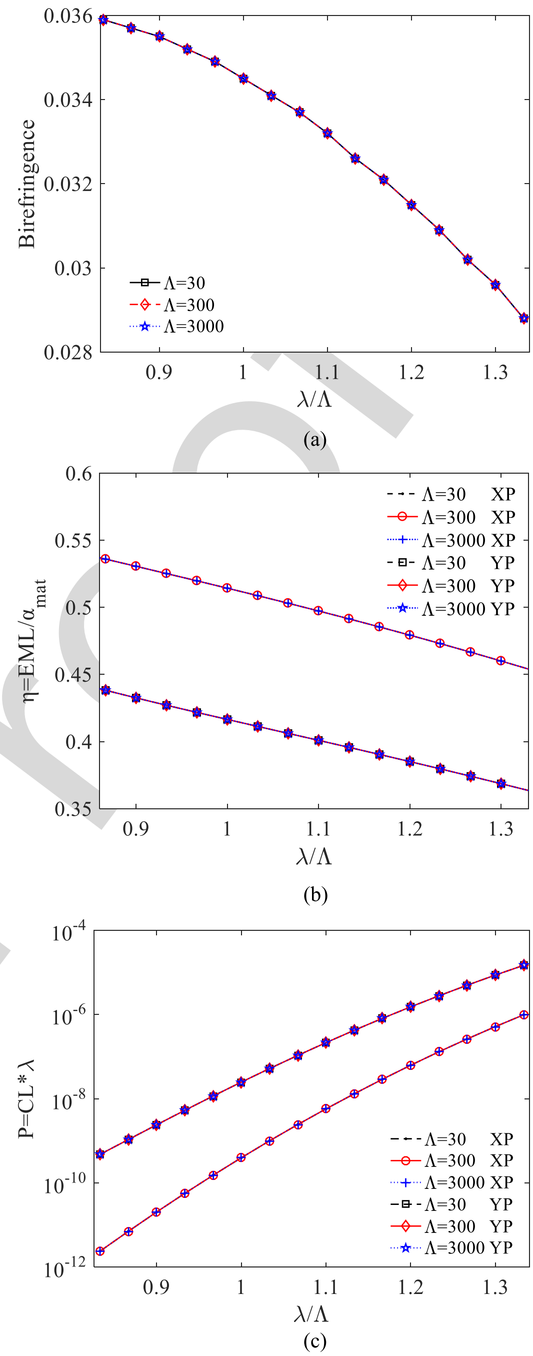

Fig. 9. Simulated (a) birefringence, (b) normalized EML, and (c) normalized CL values across THz regime as the size of the PCF reported in [22] is scaled.

V. "Scalable" PCFs

During the parameter studies, it was noticed that the variations of the CL, EML, and birefringence properties of the PS PCF with Λ were very similar to those experienced with frequency. Consequently, it was recognized that one could scale this design to other frequencies while maintaining its desirable performance. Both HRS and Topas-based PCFs were used to examine this scaling property in the THz regime. The analysis demonstrates the fact that, for different materials, the scaling principle would work as long as the chosen material has near zero dispersion in the operational frequency band. The performance indexes of the HRS-based PS PCF with $\Lambda = \{30, 100\}$ and the Topas-based PS PCF with $\Lambda = \{20, 400, 2000\}$ are shown in Fig. 8. These specific values of Λ were selected to examine whether this scaling property is maintained in the beginning, middle, and end of the THz regime. Note that the abscissa in each of the subfigures has been replaced with λ/Λ to better demonstrate these "scalable" properties.

Fig. 8(a) and (b) clearly demonstrate that the birefringence values of the design are scalable, i.e., one immediately discerns that the resulting curves are identical. This outcome confirms the fact that the scaled PS PCFs have the same birefringence property as long as the ratio of the wavelength and lattice constant is fixed for all of the operational THz frequencies. The obvious physical explanation for this behavior is that the effective index differences of the two polarization modes for different

Λ maintain the same variation. In particular, recall from Eq. (1) that n_{eff} is determined only by the PCF dimensions. Since all the dimensions were defined in proportion to Λ, n_{eff} also shares this property.

The EML values were also examined. However, they were found to be affected by the background material's characteristics, i.e., the material exhibits different properties at different frequencies. Nonetheless, it was found that by introducing the normalized quantity:

$$\eta = \frac{EML}{\alpha_{\mathrm{mat}}} \tag{4}$$

where α_{mat} is the bulk material absorption loss, one can compensate for these effects. As shown in Fig. 8(c) and (d), the corresponding normalized EML values also scale with different Λ. As a consequence, one finds that the actual EML values can be easily re-evaluated from the background material's absorption loss properties at different frequencies.

Similarly, it was found that the CL values rise with frequency even though λ/Λ is kept constant. On the other hand, it was noticed that $\mathrm{CL}*\lambda$ remains constant as long as λ/Λ is fixed. This normalized CL behavior is demonstrated in Fig. 8(e) and (f). Therefore, the CL value can also be predicted when the PCF is scaled to work at different frequencies.

To demonstrate this scaling principle can also be applied to other designs, the Topas-based PCF proposed in [22] was selected. The birefringence, normalized EML ($\mathrm{EML}/\alpha_{\mathrm{mat}}$), and normalized CL ($\mathrm{CL}*\lambda$) values are plotted in Fig. 9(a), (b), and (c), respectively. It is observed that the "scaling" principle also holds for this very different PCF design.

The discovery of this scaling principle for PCFs could significantly impact future PCF experiments. In particular, after the design and optimization of a PCF in software, its preform can be fabricated and tested before drawing it into the fiber. With this scaling property, the test results of the preform should clearly reveal the performance of the actual fiber. This outcome would help to avoid unnecessary fiber drawing if the preform does not show an acceptable performance. Subsequent efforts, including experiments, should be pursued to validate of this preform conjecture.

VI. Conclusion

A novel HRS-based PCF with a PS core was designed and optimized for THz frequencies. It was demonstrated that it exhibits improved performance characteristics when compared to its FS core counterpart. Key parameter variations were explored to explain its design principles and the tradeoffs considered in the reported system. Guidelines for tuning its properties to achieve enhanced properties for other choices emerged. The optimized design was shown to have high birefringence, low loss, and relatively flat dispersion properties across a wide band of THz frequencies, in distinct contrast to the many narrow band THz PCFs reported previously. Moreover, it was demonstrated that one can scale the PS PCF design to work at different frequencies while maintaining similar performance characteristics. The birefringence and the normalized EML (EML/α_mat) and CL ($\mathrm{CL}*\lambda$) values were shown to satisfy a scaling principle based a fixed ratio of the wavelength and the lattice constant: λ/Λ. It was determined that this behavior was directly connected to the very low dispersion properties of the background materials, HRS from 0.5 to 4.5 THz and Topas from 0.1 to 10.0 THz. This scaling principle was applied to and validated with an independently reported PCF design. It was conjectured that this scaling principle can be used to guide the redesign of similar PCF systems to other THz frequencies and could simplify future PCF experiments by predicting the performance outcome by testing the preform before the actual fiber is pulled.

References

[1] S. Cherry, "Edholm's law of bandwidth," *IEEE Spectr.*, vol. 41, no. 7, pp. 58–60, Jul. 2004.

[2] I. F. Akyildiz, J. M. Jornet, and C. Han, "Terahertz band: Next frontier for wireless communications," *Phys. Commun.*, vol. 12, pp. 16–32, Sep. 2014.

[3] D. O. Otuya, K. Kasai, M. Yoshida, T. Hirooka, and M. Nakazawa, "A single-channel 1.92 Tbit/s, 64 QAM coherent optical pulse transmission over 150 km using frequency-domain equalization," *Opt. Express*, vol. 21, no. 19, pp. 22808–28816, Sep. 2013.

[4] P.-Y. Chen, H. Huang, D. Akinwande, and A. Alù, "Graphene-based plasmonic platform for reconfigurable terahertz nanodevices," *ACS Photon.*, vol. 1, no. 8, pp. 647–654, Jul. 2014.

[5] K. Wang and D. M. Mittleman, "Metal wires for terahertz wave guiding," *Nature*, vol. 432, pp. 376–379, Nov. 2004.

[6] J. A. Harrington, R. George, and P. Pedersen, "Hollow polycarbonate waveguides with inner Cu coatings for delivery of terahertz radiation," *Opt. Express*, vol. 12, no. 21, pp. 5263–5268, Oct. 2004.

[7] G. Gallot, S. P. Jamison, R. W. McGowan, and D. Grischkowsky, "Terahertz waveguides," *J. Opt. Soc. Amer. B*, vol. 17, no. 5, pp. 851–863, May 2000.

[8] H. Han, H. Park, M. Cho, and J. Kim, "Terahertz pulse propagation in a plastic photonic crystal fiber," *Appl. Phys. Lett.*, vol. 80, no. 15, Apr. 2002, Art. no. 2634.

[9] J. Li, K. Nallappan, H. Guerboukha, and M. Skorobogatiy, "3D printed hollow core terahertz Bragg waveguides with defect layers for surface sensing applications," *Opt. Express*, vol. 25, no. 4, pp. 4126–4144, Feb. 2017.

[10] T.-Y. Yang, E. Wang, H. Jiang, Z. Hu, and K. Xie, "High birefringence photonic crystal fiber with high nonlinearity and low confinement loss," *Opt. Express*, vol. 23, no. 7, pp. 8329–8337, Apr. 2015.

[11] P. St. J. Russell, "Photonic-crystal fibers," *J. Lightw. Technol.*, vol. 24, no. 12, pp. 4729–4749, Dec. 2006.

[12] S. Atakaramians *et al.*, "THz porous fibers: Design, fabrication and experimental characterization," *Opt. Express*, vol. 17, no. 16, pp. 14053–14062, Aug. 2009.

[13] A. Aming, M. Uthman, R. Chitaree, W. Mohammed, and B. M. A. Rahman, "Design and characterization of porous core polarization maintaining photonic crystal fiber for THz guidance," *J. Lightw. Technol.*, vol. 34, no. 23, pp. 5583–5590, Dec. 2016.

[14] S. F. Kaijage, Z. B. Ouyang, and X. Jin, "Porous-core photonic crystal fiber for low loss terahertz wave guiding," *IEEE Photon. Technol. Lett.*, vol. 25, no. 15, pp. 1454–1457, Aug. 2013.

[15] M. I Hasan, S. A. Razzak, G. K. Hasanuzzaman, and M. S. Habib, "Ultralow material loss and dispersion flattened fiber for THz transmission," *IEEE Photon. Technol. Lett.*, vol. 26, no. 23, pp. 2372–2375, Dec. 2014.

[16] R. Islam, G. K. M. Hasanuzzaman, Md. S. Habib, S. Rana, and M. A. G. Khan "Low-loss rotated porous core hexagonal single-mode fiber in THz regime," *Opt. Fiber Technol.*, vol. 24, pp. 38–43, Aug. 2015.

[17] M. S. Islam, J. Sultana, J. Atai, M. R. Islam, and D. Abbott, "Design and characterization of a low-loss, dispersion-flattened photonic crystal fiber for terahertz wave propagation," *Optik*, vol. 145, pp. 398–406, Sep. 2017.

[18] G. K. M. Hasanuzzaman, M. S. Habib, S. M. A. Razzak, M. A. Hossain, and Y. Namihira, "Low loss single-mode porous-core Kagome photonic crystal fiber for THz wave guidance," *J. Lightw. Technol.*, vol. 33, no. 19, pp. 4027–4031, Oct. 2015.

[19] J. R. Folkenberg, M. D. Nielsen, N. A. Mortensen, C. Jakobsen, and H. R. Simonsen, “Polarization maintaining large mode area photonic crystal fiber,” *Opt. Express*, vol. 12, no. 5, pp. 956–960, Mar. 2004.
[20] K. Ahmed *et al.*, “Ultrahigh birefringence, ultralow material loss porous core single-mode fiber for terahertz wave guidance,” *Appl. Opt.*, vol. 56, no. 12, pp. 3477–3483, Apr. 2017.
[21] Z. Q. Wu *et al.*, “Design of highly birefringent and low-loss oligoporous-core THz photonic crystal fiber with single circular air-hole unit,” *IEEE Photon. J.*, vol. 8, no. 6, Dec. 2016, Art. no. 4502711.
[22] G. K. M. Hasanuzzaman, S. Rana, and M. S. Habib, “A novel low loss, highly birefringent photonic crystal fiber in THz regime,” *IEEE Photon. Technol. Lett.*, vol. 28, no. 8, pp. 899–902, Apr. 2016.
[23] R. Islam, M. S. Habib, G. K. M. Hasanuzzaman, S. Rana, and M. A. Sadath, “Novel porous fiber based on dual-asymmetry for low-loss polarization maintaining THz wave guidance,” *Opt. Lett.*, vol. 41, no. 3, pp. 440–445, Feb. 2016.
[24] R. Islam *et al.*, “Extremely high-birefringent asymmetric slotted-core photonic crystal fiber in THz regime,” *IEEE Photon. Technol. Lett.*, vol. 27, no. 21, pp. 2222–2225, Nov. 2015.
[25] M. R. Hasan, M. S. Anower, M. I. Hasan, and S. M. A. Razzak, “Polarization maintaining low-loss slotted core Kagome lattice THz fiber,” *IEEE Photon. Technol. Lett.*, vol. 28, no. 16, pp. 1751–1754, Aug. 2016.
[26] J. Sultana *et al.*, “Highly birefringent elliptical core photonic crystal fiber for terahertz application,” *Opt. Commun.*, vol. 407, pp. 92–96, 2018.
[27] J. Dai, J. Q. Zhang, W. L. Zhang, and D. Grischkowsky, “Terahertz time-domain spectroscopy characterization of the far-infrared absorption and index of refraction of high-resistivity, float-zone silicon,” *Opt. Soc. Amer. B*, vol. 21, no. 7, pp. 1379–1386, 2004.
[28] P. D. Cunningham *et al.*, “Broadband terahertz characterization of the refractive index and absorption of some important polymeric and organic electro-optic materials,” *J. Appl. Phys.*, vol. 109, no. 4, Feb. 2011, Art. no. 043505.
[29] J. Ballato *et al.*, “Silicon optical fiber,” *Opt. Express*, vol. 16, no. 23, pp. 18675–18683, 2008.
[30] L. Lagonigro *et al.*, “Low loss silicon fibers for photonics applications,” *Appl. Phys. Lett.*, vol. 96, pp. 0411051–0411053, 2010.
[31] O. Mitrofanov, R. James, F. A. Fernandez, T. K. Mavrogordatos, and J. A. Harrington, “Reducing transmission losses in hollow THz waveguides,” *IEEE Trans. THz Sci. Technol.*, vol. 1, no. 1, pp. 124–132, Sep. 2011.
[32] X. Y. He, C. Li, Z. H. Hu, and X. Guo, “Ultrahigh birefringent nonlinear silicon-core microfiber with two zero-dispersion wavelengths,” *J. Opt. Soc. Amer. B*, vol. 35, no. 1, pp. 122–126, 2018.

Tianyu Yang received the Bachelor’s and Master’s degrees in measurement and control technology from Hefei University of Technology, Hefei, China, in 2012 and 2016, respectively. He is currently working toward the Ph.D. degree in engineering at the University of Technology Sydney (UTS), Ultimo, NSW, Australia.

His current research interests include THz and optical photonic crystal fibers.

Q2 **Can Ding** (M’XX) received the bachelor’s degree in microelectronics from Xidian University, Xi’an, China, in 2009, and the Ph.D. degree from Macquarie University, Sydney, NSW, Australia, in 2015.

From 2012 to 2015, he was under the Cotutelle agreement between Macquarie University and Xidian University, China. During this period, he was also with Commonwealth Scientific and Industrial Research Organisation DPaS Flagship, Marsfield, Australia. From 2015 to 2017, he was a Postdoctoral Research Fellow with the University of Technology Sydney (UTS), Ultimo, NSW, Australia. He is currently a Lecturer with Global Big Data Technologies Centre, UTS. His research interests include the area of reconfigurable antenna, phase shifter, base station antenna, and THz waveguides.

Richard W. Ziolkowski (F’XX) received the B.Sc. (Hons.) (magna cum laude) degree in physics from Brown University, Providence, RI, USA, in 1974, the M.S. and Ph.D. degrees in physics from the University of Illinois at Urbana-Champaign, Urbana, IL, USA, in 1975 and 1980, respectively, and the Honorary Doctorate degree from the Technical University of Denmark, Kongens Lyngby, Denmark, in 2012. Q3

He is currently a Distinguished Professor with the University of Technology Sydney, Global Big Data Technologies Centre, Ultimo, NSW, Australia. He is also a Litton Industries John M. Leonis Distinguished Professor with the Department of Electrical and Computer Engineering and a Professor with the College of Optical Sciences, The University of Arizona, Tucson, AZ, USA. He was the Computational Electronics and Electromagnetics Thrust Area Leader with the Lawrence Livermore National Laboratory, Engineering Research Division, before joining The University of Arizona in 1990. He was the Australian DSTO Fulbright Distinguished Chair in Advanced Science and Technology from 2014 to 2015. He was a 2014 Thomas-Reuters Highly Cited Researcher. His current research interests include the application of new mathematical and numerical methods to linear and nonlinear problems dealing with the interaction of electromagnetic and acoustic waves with complex linear and nonlinear media, as well as metamaterials, metamaterial-inspired structures, and applications-specific configurations.

Dr. Ziolkowski is a Fellow of the Optical Society of America (OSA, 2006) and of the American Physical Society (APS, 2016). He served as the President of the IEEE Antennas and Propagation Society in 2005. He is also actively involved with the URSI, OSA, and SPIE professional societies.

Y. Jay Guo (F’14) received the Bachelor’s and Master’s degrees from Xidian University, Xi’an, China, in 1982 and 1984, respectively, and the Ph.D. degree from Xian Jiaotong University, Xian, in 1987. His research interests include antennas, mm-wave, and THz communications and sensing systems as well as big data. He has authored and coauthored more than 300 research papers and holds 22 patents in antennas and wireless systems. He is a Distinguished Professor and the founding Director of Global Big Data Technologies Centre at the University of Technology Sydney (UTS), Australia. Prior to this appointment in 2014, he served as a Director in CSIRO for over nine years, directing a number of ICT research portfolios. Before joining CSIRO, he held various senior leadership positions in Fujitsu, Siemens, and NEC in the U.K. He has chaired numerous international conferences.

Dr. Guo is a Fellow of the Australian Academy of Engineering and Technology, a Fellow of IET, and a member of the College of Experts of Australian Research Council. He was the recipient of a number of most prestigious Australian national awards, and was named one of the most influential engineers in Australia in 2014 and 2015. He was the International Advisory Committee Chair of IEEE VTC2017, General Chair of ISAP2015, iWAT2014 and WPMC’2014, and TPC Chair of 2010 IEEE WCNC, and 2012 and 2007 IEEE ISCIT. He served as the Guest Editor of special issues on “Antennas for Satellite Communications” and “Antennas and Propagation Aspects of 60-90GHz Wireless Communications,” both in IEEE TRANSACTIONS ON ANTENNAS AND PROPAGATION, Special Issue on “Communications Challenges and Dynamics for Unmanned Autonomous Vehicles,” IEEE JOURNAL ON SELECTED AREAS IN COMMUNICATIONS (JSAC), and Special Issue on “5G for Mission Critical Machine Communications,” IEEE NETWORK MAGAZINE.

GENERAL INSTRUCTIONS

- Authors: When accessing and uploading your corrections at the Author Gateway, please note we cannot accept new source files as corrections for your paper. Do not send new Latex, Word, or PDF files, as we cannot simply "overwrite" your paper. Please submit your corrections as an annotated PDF or as clearly written list of corrections, with location in paper, using line numbers provided on your proof. You can also upload revised graphics to the Gateway.
- Authors: Please note that once you click "approve with no changes," the proofing process is now complete and your paper will be sent for final publication and printing. Once your paper is posted on Xplore, it is considered final and the article of record. No further changes will be allowed at this point so please ensure scrutiny of your final proof.
- Authors: Unless invited or otherwise informed, overlength page charges of $260 per page are mandatory for each page in excess of seven printed pages and are required for publication. If you have any questions regarding overlength page charges, need an invoice, or have any other billing questions, please contact reprints@ieee.org as they handle these billing requests.

QUERIES

Q1. Author: Please verify that the funding information is correct.
Q2. Author: Please provide the year in which author became an IEEE Member.
Q3. Author: Please provide the year in which author became an IEEE Fellow.

A Scalable THz Photonic Crystal Fiber With Partially-Slotted Core That Exhibits Improved Birefringence and Reduced Loss

Tianyu Yang, Can Ding, *Member, IEEE*, Richard W. Ziolkowski, *Fellow, IEEE, Fellow, OSA*, and Y. Jay Guo, *Fellow, IEEE*

***Abstract*—A photonic crystal fiber (PCF) based on high resistivity silicon is reported that exhibits high birefringence, low loss, and flat dispersion characteristics across a wide bandwidth in the THz regime. Except for the center region, which remains the background dielectric, its core is occupied by a set of rectangular air slots. The material and configuration lead to high birefringence and low loss. The simulation results, which include the material losses, indicate that a birefringence value of 0.82 and a total loss of 0.011 cm^{-1}, including the effective material loss and confinement losses, are achieved at 1.0 THz. These values are a factor of ten times higher and four times lower, respectively, than many recent designs. The numerical analyses also demonstrate that the reported PCF can be scaled to any desired portion of the THz regime, while maintaining a similar birefringence, simply by changing the lattice constant. This "scalable" characteristic is shown to be applicable to other PCF designs. It could facilitate a novel way of testing THz fibers, i.e., it suggests that one only needs to test the preform to validate the performance of the fiber at higher frequencies. This outcome would significantly reduce the design complexity and the costs of PCF testing.**

***Index Terms*—Birefringence, confinement loss (CL), dispersion, effective material loss (EML), photonic crystal fiber (PCF), terahertz.**

I. Introduction

BECAUSE wireless technologies have been enhancing many aspects of people's life, the demand for access to data has dramatically increased over the last few years. It is reported that the data rates have doubled every eighteen months over the last three decades and are approaching the capacity limit of current wireless communication systems [1]. To meet the expected continuation of this growth, terahertz (THz) band communications are envisioned as the next frontier of wireless communications [2]. The THz band, which covers the spectral range from 0.1 THz to 10 THz, could effectively alleviate the spectrum scarcity and capacity limitations of current systems. While both frequency regions below (microwave) and above (optical) this band have been extensively investigated, many features of THz technology are only now being studied.

Arrays of millimeter-wave and THz sources could deliver the highly directive beams desired for these next generation systems. However, because of large losses, the propagation of THz waves in many user environments remains a significant challenge. Several approaches may yield practical guided wave solutions to realize the feed networks associated with THz arrays. One is the open air, quasi-optical transmission method [3]. It is not an effective approach because the waves are not shielded and may couple with other devices in the communication system. Substrate integrated waveguides and metallic waveguides are traditional millimeter-wave solutions. However, they also suffer from unacceptable losses in the THz regime. Feed networks based on graphene [4] are also a possible and have attracted recent attention. Nonetheless, their current fabrication difficulties and high costs remain as severe obstacles to their practical application. Stainless solid wires [5], metal-coated dielectric tubes [6], and hypodermic needles [7] can also act to guide THz waves, but they also suffer from high propagation losses.

In contrast, optical fiber-based wave guiding systems serve as promising candidates for the short range THz wave guiding needed to advance THz communication systems. For instance, signals can be suitably confined inside the fiber, thus avoiding unwanted coupling with other devices. Moreover, fibers are flexible and can be adapted to a variety of packaging requirements. Furthermore, fiber drawing techniques are mature technologies in the optical regime and could lead to easier fabrication and experiment verification of THz components. Many polymer fibers, including plastic fibers [8], Bragg fibers [9], and photonic crystal fibers (PCFs) [10], have been reported recently for THz applications.

Among these different fiber types, the PCFs are very suitable for short range THz applications. They exhibit low losses while having structural flexibility. Typical optical PCFs utilize a solid dielectric as the fiber core and insert air holes to form its cladding [11]. This structure generates the necessary index differences between the cladding and the core to promote the desired wave guiding. Recent advances in THz PCFs have

Manuscript received March 22, 2018; revised May 25, 2018; accepted May 28, 2018. This work was supported by Australian Research Council under Grant DP160102219. *(Corresponding author: Can Ding.)*

T. Yang, C. Ding, and Y. J. Guo are with the Global Big Data Technologies Centre, University of Technology Sydney, Ultimo, NSW 2007, Australia (e-mail: tianyu.yang@student.uts.edu.au; can.ding.1989@gmail.com; Jay.Guo@uts.edu.au).

R. W. Ziolkowski is with the Global Big Data Technologies Centre, University of Technology Sydney, Ultimo, NSW 2007, Australia, and also with the Department of Electrical and Computer Engineering, The University of Arizona, Tucson, AZ 85721 USA (e-mail: ziolkows@email.arizona.edu).

Color versions of one or more of the figures in this paper are available online at http://ieeexplore.ieee.org.

Digital Object Identifier 10.1109/JLT.2018.2842825

included the introduction of additional smaller air holes in the core area [12]–[14]. The aim of these porous fiber designs is to trap the majority of the wave energy in the air regions to minimize the propagation loss.

When designing THz wave guides, the most stressed factors are their loss properties, i.e., their effective material loss (EML) and confinement loss (CL). While there are other loss mechanisms, e.g., bending and scattering losses, the EML and CL losses represent the major ones in THz PCFs and are the benchmarks of this work. Many recent PCF studies have focused on achieving a low EML. An octagonal porous PCF was proposed in [14]; it was shown to have a low EML, 0.07 cm^{-1}, at a 1.0 THz operating frequency. However, the CL was not considered. Another design [15] achieved an ultra-low EML of 0.056 cm^{-1} and a CL of 0.03 cm^{-1} at 1.0 THz. A PCF employing a rotated porous hexagonal core [16] was designed to have an EML of 0.066 cm^{-1} and a CL of 4.73×10^{-4} cm^{-1} at 1.0 THz [16]. An even lower EML and CL values were realized theoretically in [17], but under an extreme assumption that cannot be realized in practice. The loss values in [18] are generally the state-of-art for THz PCFs, but that PCF was targeted for long range applications and may not be suitable for short range ones.

For short range signal transmissions, PCFs are also required to have a high birefringence in order to maintain polarization integrity over a short distance [19]. This guided wave feature is widely introduced by breaking the symmetry of either the core area or the holey cladding. For example, a rectangular porous fiber with a birefringence of 0.012 at 0.65 THz has been achieved experimentally [12]. The birefringence was realized by introducing rectangular slots into the core area. This PCF exhibited a reasonable EML below 0.25 cm^{-1} for frequencies below 0.8 THz. Similarly, squeezed elliptical holes were etched into the PCF core area in [20], achieving a birefringence on the order of 10^{-2}. An asymmetric distribution of circular air-holes was utilized in both the cladding and the core area of a PCF in [10] to achieve a high birefringence of 0.026. Introducing a single circular air-hole unit into the core area, an oligo porous-core PCF has been realized with a high birefringence of 0.03 [21]. A new kind of dual-hole unit-based porous-core hexagonal PCF was presented in [22] that yielded a low EML $= 0.1$ cm^{-1}, a low CL $= 10^{-3}$ cm^{-1}, and a high birefringence $=0.033$ at an operating frequency of 0.85 THz. A circular air hole PCF with asymmetries both in the core and the cladding was proposed in [23] and yielded an even higher birefringence $=0.045$ and a lower EML $= 0.08$ cm^{-1}. Other works based on slot cladding, circular lattice cladding, and kagome cladding were presented in [24]–[26] that also exhibited reasonable birefringence and loss values.

While most of these published works focused on a narrow band of frequencies around 1.0 THz, wide bandwidth fibers are preferred for high data capacity realizations. Consequently, another key performance factor that must be considered is dispersion. A rapidly-changing dispersion results in a significant performance variation across the bandwidth and, thus, should be avoided. Consequently, high birefringence, low loss, and flat dispersion in a wide bandwidth are all highly desirable design goals for THz fiber-based components. These often conflicting properties make achieving them all simultaneously a very challenging problem.

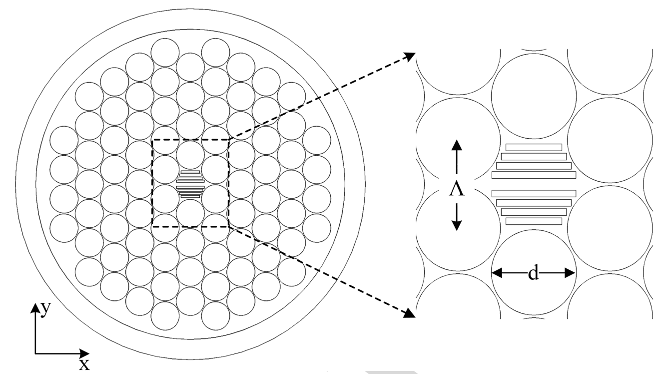

Fig. 1. Cross sectional view of the reported PCF.

A THz PCF with a partially-slotted core based on high resistivity silicon (HRS) [27] is presented in this paper. It is able to simultaneously achieve high birefringence, low loss, and flat dispersion over a broad band of frequencies. Rectangular slots are inserted into the fiber core. These air holes destroy the symmetry of the core. Nonetheless, the center area of the core remains a solid dielectric. The birefringence and loss performance can be noticeably improved with this configuration. Parameter sweeps of the key dimensions are presented to illustrate how the design is tuned to have the best performance characteristics. Numerical analyses will demonstrate that the reported PCF has a high birefringence, above 0.76, and a low total loss, below 0.04 cm^{-1} for both polarizations over a broad range from 0.9 to 1.3 THz. The dispersion variations for the two orthogonal polarized states are 0.6 ps/THz/cm and 0.5 ps/THz/cm from 0.8 to 1.1 THz, respectively. Comparisons with an analogous design based on the popular material Topas [28] further illustrate the significant advantages of the choice of HRS. Moreover, silicon has been used successfully in a variety of fiber and THz waveguide works [29]–[32].

Another contribution reported in this paper is the recognition of a "scaling property" of PCFs. In particular, by properly scaling all of the dimensions of the reported PCF, the working frequency can be shifted while maintaining its birefringence and loss properties. It is demonstrated that this scaling is generally true for different materials across a broad band of frequencies where the background material shows near zero dispersion. Additionally, another published PCF design [22] is used to illustrate that this scaling principle is universal as long as the material dispersion is near zero. Furthermore, it suggests an easier means to test PCFs in the THz regime. By only testing the preform, the performance of the PCF can be obtained without drawing it into the final fiber. This outcome would significantly reduce the cost of the development and testing of THz PCFs.

II. PCF Configuration

Fig. 1 shows the cross section of the partially-slotted (PS) PCF based on HRS. A triangular lattice distribution of five air-hole rings is used as the cladding. The distance between adjacent air holes is the lattice constant Λ. The diameter of the circular air holes in the cladding is set equal to $d = 0.95\ \Lambda$. Outside of the cladding, a matching layer is employed whose thickness is 15% of the whole diameter of the PCF. There are eight rectangular slot-shaped air holes distributed symmetrically with respect to the *x*-axis in the core area. The center of the core is solid, the background dielectric. The remainder of the core is partially slotted. The lengths L of each slot in each set of four are 0.957 Λ, 0.851 Λ, 0.745 Λ, and 0.638 Λ, respectively, from its middle to its edge. The width of all of the slots is $\mathrm{W} = 0.04\ \Lambda$ and the distance between any two adjacent slots is $\mathrm{D} = 0.105\ \Lambda$. The dielectric in the core center has a fixed width of 0.132 Λ. Note that all the dimensions have been described in terms of the lattice constant Λ. This choice is an optimal way to describe the PCF; it facilitates the scaling property that will be introduced below. The optimized lattice constant value was found to be $\Lambda = 100\ \mu$m.

As noted, both HRS [27] and Topas [28] were considered as the background dielectric material. On one hand, we have found that HRS, whose material absorption loss is less than 0.015 cm^{-1} below 1.5 THz and whose refractive index $\mathrm{n} = 3.417$ from 0.5 to 4.5 THz, leads to superior birefringence and loss properties across a wider band. On the other hand, a number of PCF studies have used Topas because of its low bulk material absorption loss $<0.2\ \mathrm{cm}^{-1}$ and stable refractive index $\mathrm{n} = 1.5258$ below 1.0 THz. Since the refractive indexes of these two materials are different, the Topas-based PCF parameters must be obtained separately. It was found that the same PS design was optimized with Topas simply by setting $\Lambda = 400\ \mu$m and $\mathrm{W} = 0.078\ \Lambda$.

III. Numerical Simulations

The simulations in this work were conducted with the commercial software COMSOL Multiphysics. It is based on the full-vector finite element method (FEM). Perfectly matched layer (PML) boundary conditions were employed.

To demonstrate the superiority of the PS configuration over the commonly known fully-slotted (FS) configuration [24]–[26], simulations were performed for both HRS-based and Topas-based PCFs with and without the center slot. For these comparison PCF designs to be commensurate with published works, the lattice constant Λ was set to be 100 μm.

The HRS-based FS PCF is attained simply by adding a slot with the optimized dimensions: $L \times W = 1.064\ \Lambda \times 0.04\ \Lambda$ to the corresponding FS design. The electric field distributions in the central regions of the HRS-based PS and FS PCFs are presented in Fig. 2 for both the X-polarized (X-pol) and Y-polarized (Y-pol) modes. As illustrated, the differences between the HRS-based PS and FS PCFs are not significant. This is simply due to the fact that the slot is quite narrow. Nevertheless, quantitative comparisons based on the birefringence and loss values given below demonstrate that the PS configuration is superior to the FS one. On the other hand, it is clear that the X-pol fields are more strongly confined to the core than the Y-pol ones. In fact, more than two to three times the power is localized in the core for the X-pol mode in comparison to the Y-pol mode over the frequencies of interest.

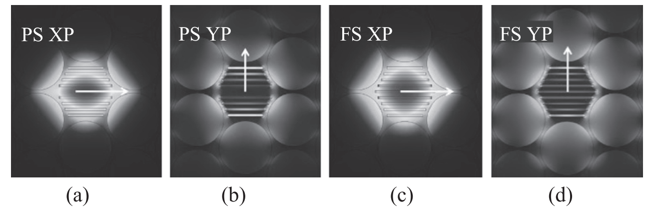

Fig. 2. The magnitude of the electric field distributions at 1.0 THz for the HRS-based PCFs. (a) X- and (b) Y-pol modes of the PS PCF. (c) X- and (d) Y-pol modes of the FS PCF. (The arrows represent the direction of the electric field vector. The color spectrum for each subplot represents the same power levels (dark red is maximum; dark blue is minimum).)

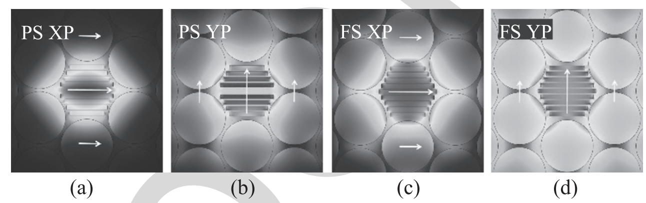

Fig. 3. The magnitude of the electric field distribution at 1.0 THz for the Topas-based PCFs. (a) X- and (b) Y-pol modes of the PS PCF. (c) X- and (d) Y-pol modes of the FS PCF. (The arrows represent the direction of the electric field vector. The color spectrum for each subplot represents the same power levels (dark red is maximum; dark blue is minimum).)

Similarly, the central slot for the Topas-based FS PCF has the optimized dimensions: $L \times W = 1.064\ \Lambda \times 0.078\ \Lambda$. The electric field distributions in the central regions of both the PS and FS designs are presented in Fig. 3. The X- and Y-pol modes of the FS PCF presented in Fig. 3(c) and (d) clearly show that more power is distributed in its cladding when compared to the same modes for the PS PCF shown in Fig. 3(a) and (b). Similarly, it is also clear that more power is present in the central region of the PS design.

These large differences in the behaviors of the PS and FS Topas designs arise from their wider slots and their lower substrate index contrast. These features lead to an effective index of the core region which is relatively low and, hence, poorer confinement there. Nonetheless, the higher percentage of the dielectric remaining in the core of both the HRS- and Topas-based PS structures improves the index contrast between it and the cladding. This leads to improved field confinement in the PS cores. Consequently, a much higher birefringence is attained, for example, with the Topas-based PS PCF (0.069) in comparison to the FS PCF (0.025) at 1 THz.

As is also observed in Fig. 3, the electric field of the X-pol mode is strongly concentrated in the core. In contrast, a noticeable proportion of the electric field appears in the cladding for the Y-pol mode. Moreover, the electric field of the Y-pol mode remains mainly in the air slots; very little is distributed into the dielectric. On the other hand, the X-pol electric field has no apparent preferences between the air slots or dielectric in the core region.

The key performance indexes of the HRS-based PS and FS PCFs: the CL, EML, birefringence, and dispersion values, are compared in Fig. 4 as functions of the source frequency. Following [18], the CL values shown in Fig. 4(a) were

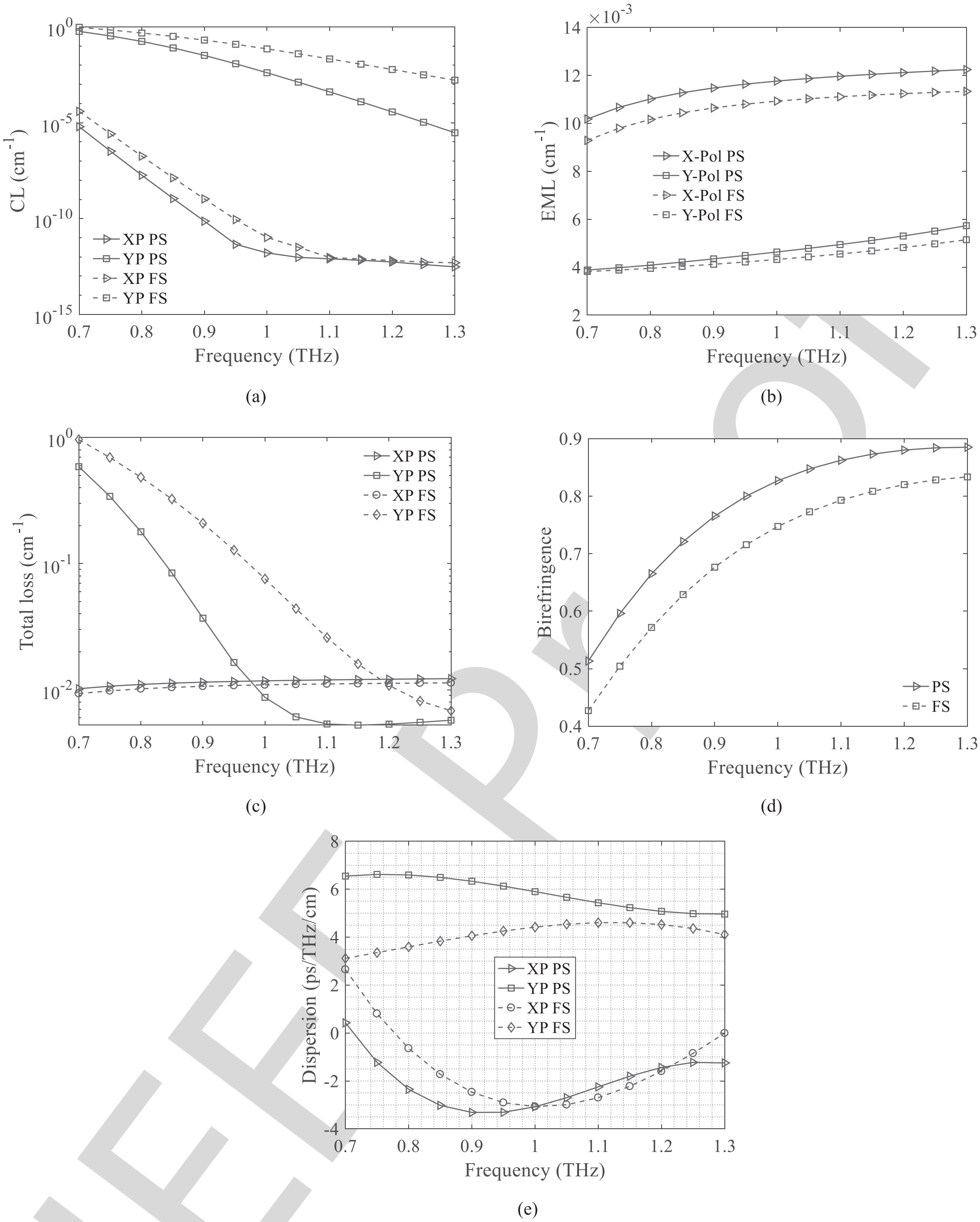

Fig. 4. Comparison of the simulated performance characteristics of the X- and Y-pol modes of the HRS-based PS (solid lines) and FS (dashed lines) PCFs. The (a) CL, (b) EML, (c) total loss, (d) birefringence, and (e) dispersion values as functions of the source frequency. (Note: XP denotes X-pol; YP denotes Y-pol.)

calculated as

$$L_c\left(\mathrm{cm}^{-1}\right) = \frac{4\pi f}{c} \times Im\ [n_{\mathrm{eff}}], \qquad (1)$$

where c is the speed of light in vacuum and $\mathrm{Im}[n_{\mathrm{eff}}]$ is the imaginary part of the effective refractive index. As observed in Fig. 4(a), the CL values for both the X- and Y-pol modes are smaller in the PS PCF. Furthermore, the X-pol CL values are observed to be significantly smaller than the Y-pol ones for both the PS and FS PCFs.

The reason that the CL values in the X-pol modes are significantly lower than the Y-pol modes arises from the much stronger confinement in the core in the former and the presence of the air-filled slots in the core. One finds that about half the X-pol power in the core is associated with the slot regions which are filled with air. This is actually discernable in Fig. 2(a) and (b). Consequently, the values of $\mathrm{Im}[n_{\mathrm{eff}}]$ are tiny. While Fig. 2(b) and (d) show the fields in the slots are much larger than their surrounding dielectric, they also illustrate the much poorer confinement in the core. Thus, while the Y-pol values of $\mathrm{Im}[n_{\mathrm{eff}}]$ are relatively small, they are not tiny. Moreover, because of the nature of the Y-pol band-gap structure formed by the slots, the defect region in the PS structure (i.e., the HRS center of the core) causes the fields outside of the core to be lower than those in the FS structure. This smaller confinement thus causes the Y-pol Im$[n_{\rm eff}]$ values to be larger in the FS case. The slightly different X-pol CL values for the PS and FS structures arise from the slightly poorer confinement observed between Fig. 2(a) and (c).

The EMLs of both modes and PCFs are plotted in Fig. 4(b). They were obtained with the expression

$$\alpha_{\rm eff}\left(\text{cm}^{-1}\right) = \frac{\left(\frac{\varepsilon_0}{\mu_0}\right)^{\frac{1}{2}} \int_{\rm mat}\ n_{\rm mat}\ \alpha_{\rm mat}\ |E|^2\ dA}{2\int_{All}\ S_z\ dA}, \quad (2)$$

where ε_0 and μ_0 are the permittivity and permeability of vacuum, $n_{\rm mat}$ is the refractive index of the background material, $\alpha_{\rm mat}$ is the bulk material absorption loss, E is the modal electric field, and S_z is the Poynting vector projection in the Z direction. As shown in Fig. 4(b), the EML values of the PS PCF are slightly higher than those of the FS design for both the two polarized modes. This outcome is simply due to the fact that the PS PCF has a slightly larger fraction of the dielectric in the core area. It also is observed that the X-pol EMLs are larger than the Y-pol EMLs. This behavior is due to the fact that the Y-pol electric field is concentrated mainly in the air slots (see Fig. 2).

Although the EML values are slightly higher for PS PCF, its CL values are lower. The total losses, considering both the EML and CL values, are presented in Fig. 4(c). These results demonstrate that the PS PCF has a much smaller loss for the Y-pol mode and a comparable loss for the X-pol mode when compared to those of the FS PCF. Because the total loss is the combination of the CL and EML values, we will only report the total loss for the parameter studies below.

The birefringence, *B*, is calculated as

$$B = |n_x - n_y|, \quad (3)$$

where n_x and n_y are the effective modal refractive indexes for the X- and Y-pol modes, respectively. The simulated birefringence values for both PCFs are given in Fig. 4(d). It is noted immediately that the birefringence of both the PS and FS PCFs is very high. Moreover, there is an enhancement of the birefringence achieved by introducing the PS core. Specifically, the birefringence is improved from 0.42 to 0.51 and from 0.83 to 0.88 at 0.7 THz and 1.3 THz, respectively. The real parts of the indexes completely dominate the birefringence calculation (3). The presence of the HRS dielectric in the center of the core of the PS structure causes the value of Re$(n_{\rm eff})$ in the X-pol case to be larger than it is in the FS structure.

Fig. 4(e) shows the dispersion curves versus frequency for both PCFs and their X- and Y-pol modes. Since the material dispersion of the HRS is negligible within the 0.5–4.5 THz frequency band, these curves basically represent the effects of waveguide dispersion. The latter is calculated with the expression [18]:

$$\beta_2 = \frac{2}{c}\frac{dn_{\rm eff}}{d\omega} + \frac{\omega}{c}\frac{d^2 n_{\rm eff}}{d\omega} \quad (4)$$

where $n_{\rm eff}$ is specifically the effective refractive index of the fundamental mode and $\omega = 2\pi f$ is its angular center frequency. It can be seen that the dispersion curve of the PS PCF is much flatter across the frequencies of interest in comparison to the FS PCF one. In particular, the variations of the dispersion curve for both polarization states of the PS PCF are low: -2.8 ± 0.6 ps/THz/cm for the X-pol mode and 6.0 ± 0.5 ps/THz/cm for the Y-pol mode from 0.8 to 1.1 THz. It is found that the values of Re$(n_{\rm eff})$ for the X-pol mode for both the PS and FS structures are larger for than those of the Y-pol mode. The slopes of the X-pol values for both structures are decreasing with increasing frequency. The slopes of the Y-pol values are positive with increasing frequency. On the other hand, the values of Im$(n_{\rm eff})$ are decreasing with frequency for both modes and both structures, but they are more than two orders of magnitude smaller than the real values. These features of the effective index values lead to the exhibited negative dispersion values for the X-pol case and the positive ones for the Y-pol case.

In summary, all of these performance characteristic results clearly demonstrate the superiority of the PS configuration.

IV. Parameter Studies

Parameter sweeps were conducted to optimize the HRS-based PS PCF design. Various compromises between the different performance indexes allow one to meet different specifications. A summary of the main design parameter results provide guidelines for configuring this PCF for any of its many potential applications.

A. *Effects of the Lattice Constant* Λ

The most important design parameter is the lattice constant, Λ, particularly since all of the PCF dimensions are defined proportional to it. The simulated total loss, birefringence, and dispersion values for different Λ values are plotted in Fig. 5(a) to (c), respectively. As shown in Fig. 5(a), the total loss for the Y-pol mode decreases rapidly with an increase of lattice constant Λ. For this mode, the loss is dominated by the CL values, which are more sensitive to the dimensions of the structure. On the other hand, the total loss of the X-pol mode remains basically constant. The latter occurs because its loss is dominated by the EML, and the HRS loss value varies little across the frequencies of interest.

Fig. 5(b) illustrates the changes in the birefringence values. They increase as both the lattice constant Λ and the operating frequency increase. As Fig. 5(c) illustrates, the dispersion values for the different Λ values can exhibit rather large variations if the lattice constant is not chosen properly.

An appropriate compromise amongst all of the performance characteristic values is obtained by selecting $\Lambda = 100\ \mu$m. This HRS-based PS PCF has low losses, i.e., below 0.04 cm^{-1}, for both polarizations from 0.9 to 1.3 THz. It has birefringence values above 0.76 across this frequency range. On the other hand, its dispersion values for the less-confined X-pol mode are -2.3 ± 1.0 (43%), while they are 5.7 ± 0.7, i.e., only a 12% variation for the more-confined Y-pol mode across the same frequency range.

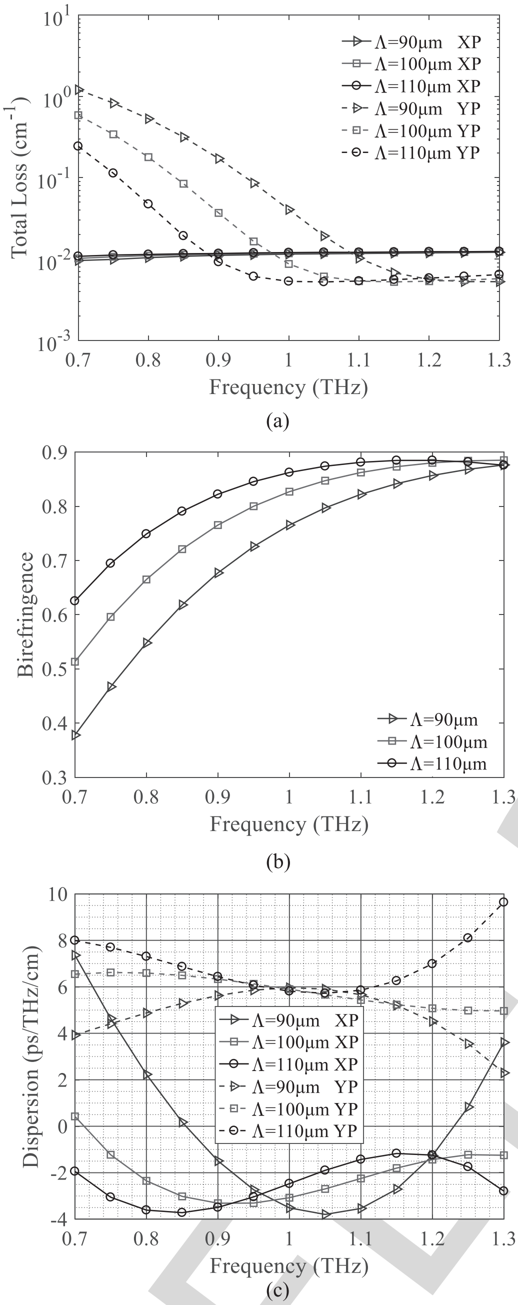

Fig. 5. Simulated (a) total loss, (b) birefringence, and (c) dispersion values of the PS PCF across a wide frequency range for different Λ values.

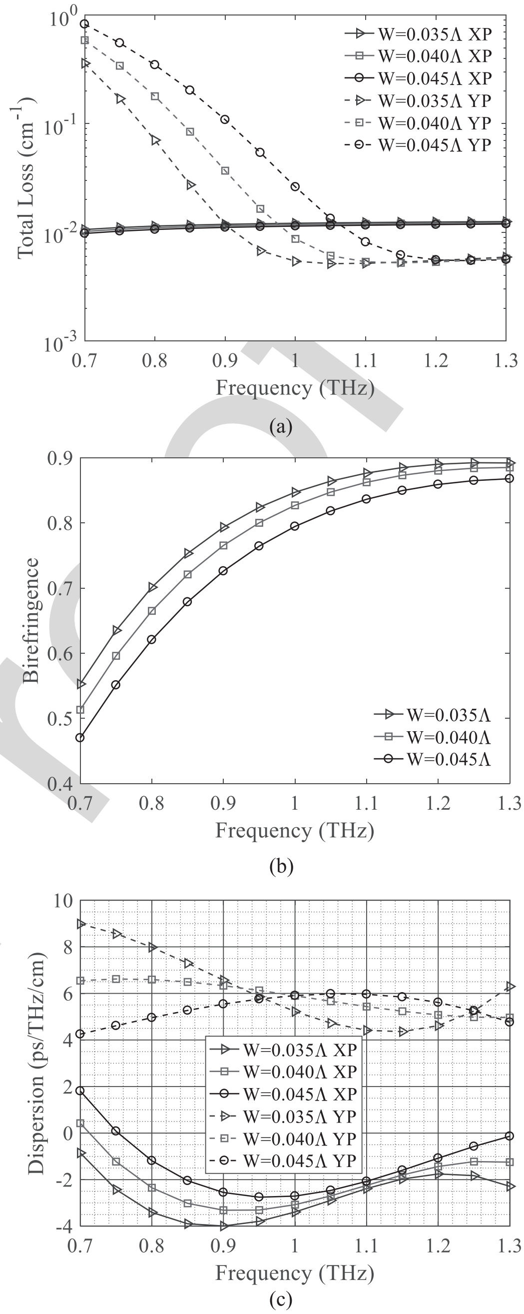

Fig. 6. Simulated (a) total loss, (b) birefringence, and (c) dispersion values of the PS PCF with $\Lambda = 100$ μm for different W across a wide frequency range.

B. Effects of the Slot Width

The slot width, W, also has a significant influence on the performance characteristics. A parameter sweep of W was conducted with all of the other dimensions remaining fixed, notably with $\Lambda = 100$ μm. The resulting variations of total loss, birefringence, and dispersion are presented in Fig. 6(a) to (c), respectively.

As observed in Fig. 6(a), the TL values are essentially constant for the X-pol modes. Because the fields are strongly confined to the core region, there is little TL variation encountered as the slot size increases. On the other hand, more loss is incurred for the Y-pol mode at lower frequencies for larger W because the fields in the HRS become larger as the edges of the slots are closer together and more strongly coupled. As the frequency increases and, hence, the wavelength decreases, this coupling decreases and the TL values decrease. The TL values eventually saturate at some higher frequency as this coupling becomes minor.

Fig. 6(b) demonstrates that the birefringence increases as W decreases and the frequency increases. This effect again arises because a higher real part of the effective n_x is realized when more HRS present for the smaller W values and a higher contrast between the core and the cladding occurs for smaller wavelengths. Fig. 6(c) indicates that the dispersion values for the

TABLE I
PERFORMANCE COMPARISONS BETWEEN THE STATES-OF-ART PCFS AND THE PCF REPORTED IN THIS WORK

Works	Confinement loss(cm^{-1})	EML (cm^{-1})	Total loss (cm^{-1})	Birefringence	Dispersion variation (ps/THz/cm)
[14]	-	0.07	-	-	-
[15]	0.03	0.057	0.087	-	0.18
[16]	$10^{-3.5}$	0.066	0.067	-	0.3
[18]	0.0012	0.035	0.036	-	0.09
[24]	0.008	0.07	0.078	0.075	0.5
[22]	10^{-3}	0.1	0.11	0.033	-
[23]	-	0.08	-	0.045	0.5
[21]	3.5	0.1	3.51	0.03	0.3
[17]	$10^{-3.7}$	0.034	0.035	0.001	0.09
[26]	10^{-9}	0.05	0.05	0.086	0.07
Topas PS YP	10^{-6}	0.071	0.071	0.069	0.07
Topas PS XP	10^{-12}	0.11	0.11		0.06
HRS PS YP	0.0041	0.0046	0.0087	0.82	0.5
HRS PS XP	10^{-12}	0.011	0.011		0.6

X-pol mode experience only minor variations for different W values, but experience larger ones for the Y-pol mode.

Consequently, we elected to set W = 0.04 Λ (4.0 μm) as the optimized value. It produces high birefringence and low loss around 1.0 THz and has the smallest variations in the dispersion values.

Finally, we note that the diameter of the circular air hole, d, also has a direct impact on the performance characteristics. A larger d yields a better confinement of the field, which in turn leads to higher birefringence and lower loss values. Nevertheless, the fabrication of the PCF is more difficult when the difference between d and Λ becomes smaller. Therefore, d was chosen to be 0.95 Λ for the optimized design as a tradeoff between of the performance values and the anticipated fabrication complexity.

C. Performance Comparison

As a final comparison between the HRS- and Topas-based PS PCFs, Fig. 7(a) and (b) present their simulated total loss and birefringence values for their optimized designs, respectively. It is noted that the Y-pol loss of the HRS-based PS PCF is quite high at the lowest frequencies, but achieves much lower loss for both two polarizations when the frequency is above 0.9 THz. On the other hand, Fig. 7(b) demonstrates conclusively that the birefringence values achieved by the HRS-based PS PCF are an order of magnitude higher than those of the corresponding Topas-based design.

In summary, the optimized HRS-based PS PCF performance characteristics are compared with the reported state-of-art PCFs as listed in Table I. Our design has the smallest loss, being nearly 4 times lower than the other designs. The birefringence achieved is remarkably ~10 times higher than all of the reported designs.

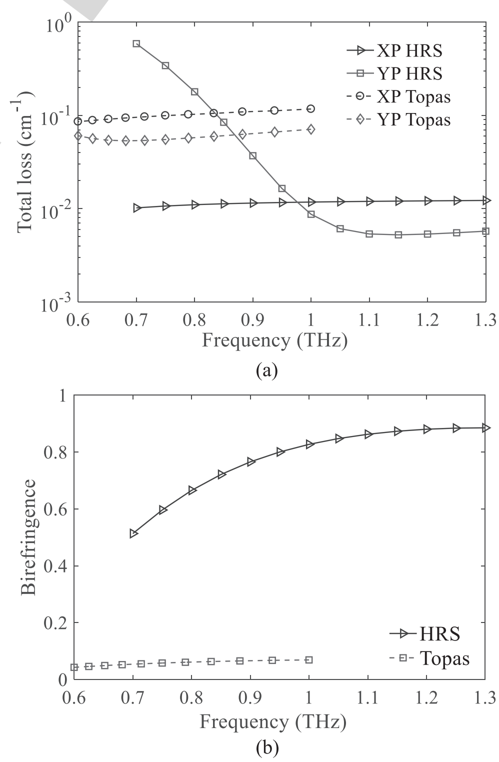

Fig. 7. Comparison of the simulated (a) total loss and (b) birefringence values of the optimized HRS- and TOPAS-based PS PCFs as functions of the source frequency.

On the other hand, the variation of the dispersion values is comparable. Furthermore, our design also provides these superior properties over a wide bandwidth rather than being limited to operation in a narrow band of frequencies around 1.0 THz.

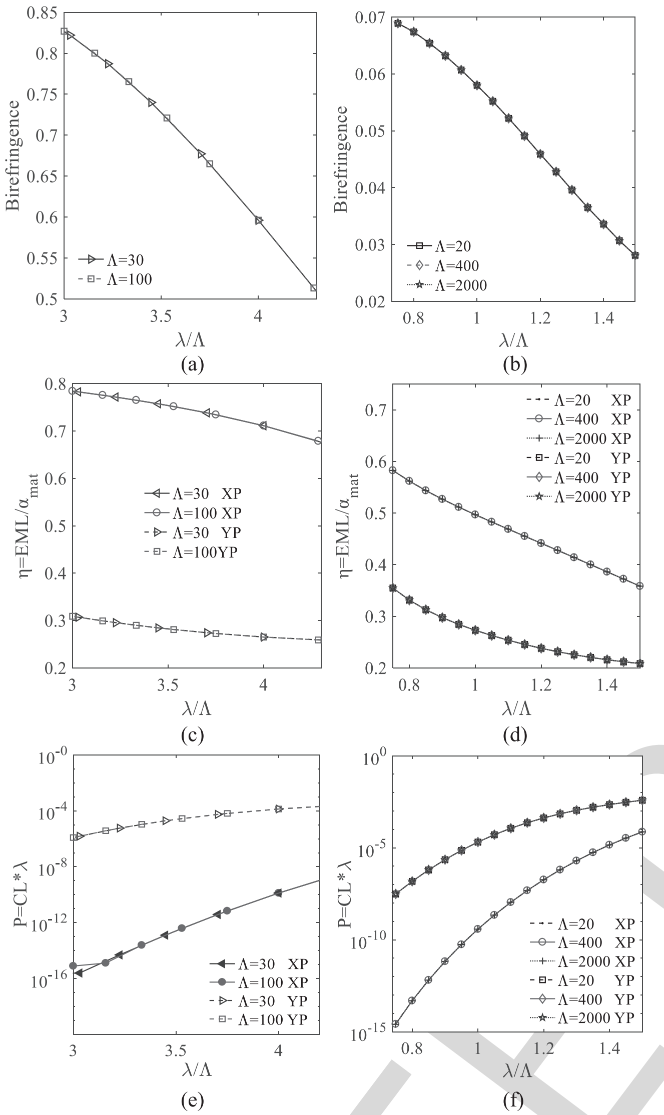

Fig. 8. Simulated (a), (b) birefringence, (c), (d) normalized EML, and (e), (f) normalized CL values across THz regime as the size of the HRS and Topas PCFs are scaled respectively. (Note that the units of Λ are micrometers.)

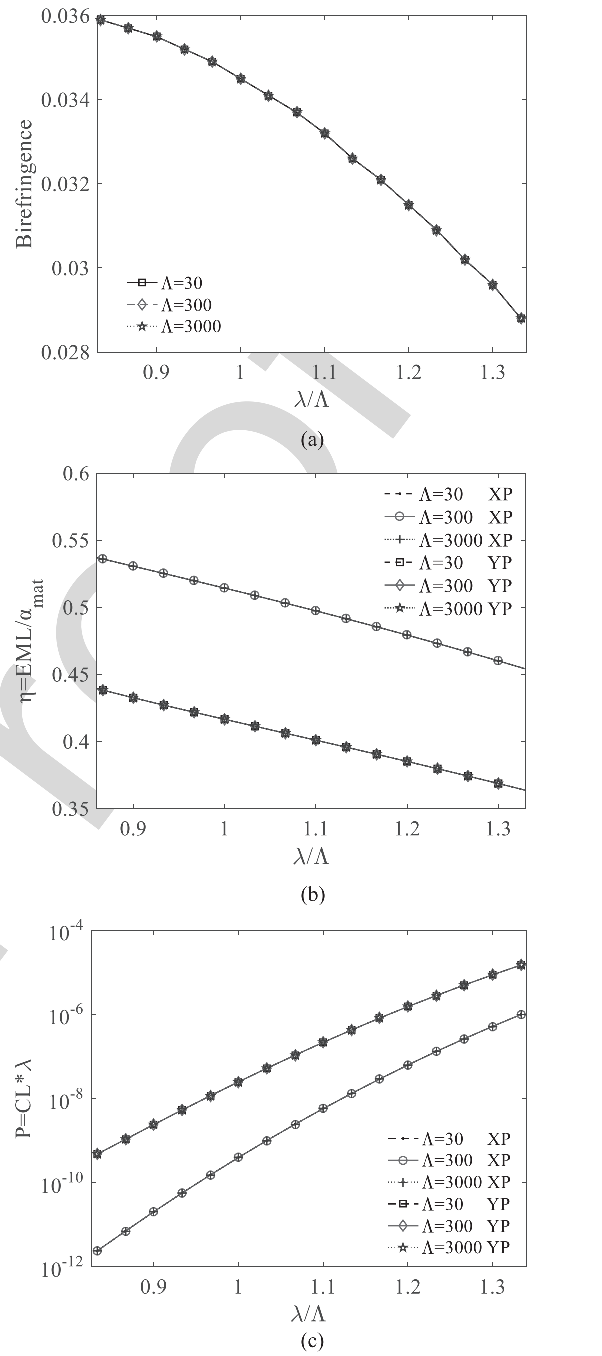

Fig. 9. Simulated (a) birefringence, (b) normalized EML, and (c) normalized CL values across THz regime as the size of the PCF reported in [22] is scaled.

V. “Scalable” PCFs

During the parameter studies, it was noticed that the variations of the CL, EML, and birefringence properties of the PS PCF with Λ were very similar to those experienced with frequency. Consequently, it was recognized that one could scale this design to other frequencies while maintaining its desirable performance. Both HRS and Topas-based PCFs were used to examine this scaling property in the THz regime. The analysis demonstrates the fact that, for different materials, the scaling principle would work as long as the chosen material has near zero dispersion in the operational frequency band. The performance indexes of the HRS-based PS PCF with $\Lambda = \{30, 100\}$ and the Topas-based PS PCF with $\Lambda = \{20, 400, 2000\}$ are shown in Fig. 8. These specific values of Λ were selected to examine whether this scaling property is maintained in the beginning, middle, and end of the THz regime. Note that the abscissa in each of the subfigures has been replaced with λ/Λ to better demonstrate these “scalable” properties.

Fig. 8(a) and (b) clearly demonstrate that the birefringence values of the design are scalable, i.e., one immediately discerns that the resulting curves are identical. This outcome confirms the fact that the scaled PS PCFs have the same birefringence property as long as the ratio of the wavelength and lattice constant is fixed for all of the operational THz frequencies. The obvious physical explanation for this behavior is that the effective index differences of the two polarization modes for different

Λ maintain the same variation. In particular, recall from Eq. (1) that n_{eff} is determined only by the PCF dimensions. Since all the dimensions were defined in proportion to Λ, n_{eff} also shares this property.

The EML values were also examined. However, they were found to be affected by the background material's characteristics, i.e., the material exhibits different properties at different frequencies. Nonetheless, it was found that by introducing the normalized quantity:

$$\eta = \frac{EML}{\alpha_{\mathrm{mat}}} \tag{4}$$

where α_{mat} is the bulk material absorption loss, one can compensate for these effects. As shown in Fig. 8(c) and (d), the corresponding normalized EML values also scale with different Λ. As a consequence, one finds that the actual EML values can be easily re-evaluated from the background material's absorption loss properties at different frequencies.

Similarly, it was found that the CL values rise with frequency even though λ/Λ is kept constant. On the other hand, it was noticed that CL∗λ remains constant as long as λ/Λ is fixed. This normalized CL behavior is demonstrated in Fig. 8(e) and (f). Therefore, the CL value can also be predicted when the PCF is scaled to work at different frequencies.

To demonstrate this scaling principle can also be applied to other designs, the Topas-based PCF proposed in [22] was selected. The birefringence, normalized EML (EML/α_{mat}), and normalized CL (CL∗λ) values are plotted in Fig. 9(a), (b), and (c), respectively. It is observed that the "scaling" principle also holds for this very different PCF design.

The discovery of this scaling principle for PCFs could significantly impact future PCF experiments. In particular, after the design and optimization of a PCF in software, its preform can be fabricated and tested before drawing it into the fiber. With this scaling property, the test results of the preform should clearly reveal the performance of the actual fiber. This outcome would help to avoid unnecessary fiber drawing if the preform does not show an acceptable performance. Subsequent efforts, including experiments, should be pursued to validate of this preform conjecture.

VI. Conclusion

A novel HRS-based PCF with a PS core was designed and optimized for THz frequencies. It was demonstrated that it exhibits improved performance characteristics when compared to its FS core counterpart. Key parameter variations were explored to explain its design principles and the tradeoffs considered in the reported system. Guidelines for tuning its properties to achieve enhanced properties for other choices emerged. The optimized design was shown to have high birefringence, low loss, and relatively flat dispersion properties across a wide band of THz frequencies, in distinct contrast to the many narrow band THz PCFs reported previously. Moreover, it was demonstrated that one can scale the PS PCF design to work at different frequencies while maintaining similar performance characteristics. The birefringence and the normalized EML (EML/α_mat) and CL (CL∗λ) values were shown to satisfy a scaling principle based a fixed ratio of the wavelength and the lattice constant: λ/Λ. It was determined that this behavior was directly connected to the very low dispersion properties of the background materials, HRS from 0.5 to 4.5 THz and Topas from 0.1 to 10.0 THz. This scaling principle was applied to and validated with an independently reported PCF design. It was conjectured that this scaling principle can be used to guide the redesign of similar PCF systems to other THz frequencies and could simplify future PCF experiments by predicting the performance outcome by testing the preform before the actual fiber is pulled.

References

[1] S. Cherry, "Edholm's law of bandwidth," *IEEE Spectr.*, vol. 41, no. 7, pp. 58–60, Jul. 2004.

[2] I. F. Akyildiz, J. M. Jornet, and C. Han, "Terahertz band: Next frontier for wireless communications," *Phys. Commun.*, vol. 12, pp. 16–32, Sep. 2014.

[3] D. O. Otuya, K. Kasai, M. Yoshida, T. Hirooka, and M. Nakazawa, "A single-channel 1.92 Tbit/s, 64 QAM coherent optical pulse transmission over 150 km using frequency-domain equalization," *Opt. Express*, vol. 21, no. 19, pp. 22808–28816, Sep. 2013.

[4] P.-Y. Chen, H. Huang, D. Akinwande, and A. Alù, "Graphene-based plasmonic platform for reconfigurable terahertz nanodevices," *ACS Photon.*, vol. 1, no. 8, pp. 647–654, Jul. 2014.

[5] K. Wang and D. M. Mittleman, "Metal wires for terahertz wave guiding," *Nature*, vol. 432, pp. 376–379, Nov. 2004.

[6] J. A. Harrington, R. George, and P. Pedersen, "Hollow polycarbonate waveguides with inner Cu coatings for delivery of terahertz radiation," *Opt. Express*, vol. 12, no. 21, pp. 5263–5268, Oct. 2004.

[7] G. Gallot, S. P. Jamison, R. W. McGowan, and D. Grischkowsky, "Terahertz waveguides," *J. Opt. Soc. Amer. B*, vol. 17, no. 5, pp. 851–863, May 2000.

[8] H. Han, H. Park, M. Cho, and J. Kim, "Terahertz pulse propagation in a plastic photonic crystal fiber," *Appl. Phys. Lett.*, vol. 80, no. 15, Apr. 2002, Art. no. 2634.

[9] J. Li, K. Nallappan, H. Guerboukha, and M. Skorobogatiy, "3D printed hollow core terahertz Bragg waveguides with defect layers for surface sensing applications," *Opt. Express*, vol. 25, no. 4, pp. 4126–4144, Feb. 2017.

[10] T.-Y. Yang, E. Wang, H. Jiang, Z. Hu, and K. Xie, "High birefringence photonic crystal fiber with high nonlinearity and low confinement loss," *Opt. Express*, vol. 23, no. 7, pp. 8329–8337, Apr. 2015.

[11] P. St. J. Russell, "Photonic-crystal fibers," *J. Lightw. Technol.*, vol. 24, no. 12, pp. 4729–4749, Dec. 2006.

[12] S. Atakaramians *et al.*, "THz porous fibers: Design, fabrication and experimental characterization," *Opt. Express*, vol. 17, no. 16, pp. 14053–14062, Aug. 2009.

[13] A. Aming, M. Uthman, R. Chitaree, W. Mohammed, and B. M. A. Rahman, "Design and characterization of porous core polarization maintaining photonic crystal fiber for THz guidance," *J. Lightw. Technol.*, vol. 34, no. 23, pp. 5583–5590, Dec. 2016.

[14] S. F. Kaijage, Z. B. Ouyang, and X. Jin, "Porous-core photonic crystal fiber for low loss terahertz wave guiding," *IEEE Photon. Technol. Lett.*, vol. 25, no. 15, pp. 1454–1457, Aug. 2013.

[15] M. I Hasan, S. A. Razzak, G. K. Hasanuzzaman, and M. S. Habib, "Ultra-low material loss and dispersion flattened fiber for THz transmission," *IEEE Photon. Technol. Lett.*, vol. 26, no. 23, pp. 2372–2375, Dec. 2014.

[16] R. Islam, G. K. M. Hasanuzzaman, Md. S. Habib, S. Rana, and M. A. G. Khan "Low-loss rotated porous core hexagonal single-mode fiber in THz regime," *Opt. Fiber Technol.*, vol. 24, pp. 38–43, Aug. 2015.

[17] M. S. Islam, J. Sultana, J. Atai, M. R. Islam, and D. Abbott, "Design and characterization of a low-loss, dispersion-flattened photonic crystal fiber for terahertz wave propagation," *Optik*, vol. 145, pp. 398–406, Sep. 2017.

[18] G. K. M. Hasanuzzaman, M. S. Habib, S. M. A. Razzak, M. A. Hossain, and Y. Namihira, "Low loss single-mode porous-core Kagome photonic crystal fiber for THz wave guidance," *J. Lightw. Technol.*, vol. 33, no. 19, pp. 4027–4031, Oct. 2015.

[19] J. R. Folkenberg, M. D. Nielsen, N. A. Mortensen, C. Jakobsen, and H. R. Simonsen, “Polarization maintaining large mode area photonic crystal fiber,” *Opt. Express*, vol. 12, no. 5, pp. 956–960, Mar. 2004.

[20] K. Ahmed *et al.*, “Ultrahigh birefringence, ultralow material loss porous core single-mode fiber for terahertz wave guidance,” *Appl. Opt.*, vol. 56, no. 12, pp. 3477–3483, Apr. 2017.

[21] Z. Q. Wu *et al.*, “Design of highly birefringent and low-loss oligoporous-core THz photonic crystal fiber with single circular air-hole unit,” *IEEE Photon. J.*, vol. 8, no. 6, Dec. 2016, Art. no. 4502711.

[22] G. K. M. Hasanuzzaman, S. Rana, and M. S. Habib, “A novel low loss, highly birefringent photonic crystal fiber in THz regime,” *IEEE Photon. Technol. Lett.*, vol. 28, no. 8, pp. 899–902, Apr. 2016.

[23] R. Islam, M. S. Habib, G. K. M. Hasanuzzaman, S. Rana, and M. A. Sadath, “Novel porous fiber based on dual-asymmetry for low-loss polarization maintaining THz wave guidance,” *Opt. Lett.*, vol. 41, no. 3, pp. 440–445, Feb. 2016.

[24] R. Islam *et al.*, “Extremely high-birefringent asymmetric slotted-core photonic crystal fiber in THz regime,” *IEEE Photon. Technol. Lett.*, vol. 27, no. 21, pp. 2222–2225, Nov. 2015.

[25] M. R. Hasan, M. S. Anower, M. I. Hasan, and S. M. A. Razzak, “Polarization maintaining low-loss slotted core Kagome lattice THz fiber,” *IEEE Photon. Technol. Lett.*, vol. 28, no. 16, pp. 1751–1754, Aug. 2016.

[26] J. Sultana *et al.*, “Highly birefringent elliptical core photonic crystal fiber for terahertz application,” *Opt. Commun.*, vol. 407, pp. 92–96, 2018.

[27] J. Dai, J. Q. Zhang, W. L. Zhang, and D. Grischkowsky, “Terahertz time-domain spectroscopy characterization of the far-infrared absorption and index of refraction of high-resistivity, float-zone silicon,” *Opt. Soc. Amer. B*, vol. 21, no. 7, pp. 1379–1386, 2004.

[28] P. D. Cunningham *et al.*, “Broadband terahertz characterization of the refractive index and absorption of some important polymeric and organic electro-optic materials,” *J. Appl. Phys.*, vol. 109, no. 4, Feb. 2011, Art. no. 043505.

[29] J. Ballato *et al.*, “Silicon optical fiber,” *Opt. Express*, vol. 16, no. 23, pp. 18675–18683, 2008.

[30] L. Lagonigro *et al.*, “Low loss silicon fibers for photonics applications,” *Appl. Phys. Lett.*, vol. 96, pp. 0411051–0411053, 2010.

[31] O. Mitrofanov, R. James, F. A. Fernandez, T. K. Mavrogordatos, and J. A. Harrington, “Reducing transmission losses in hollow THz waveguides,” *IEEE Trans. THz Sci. Technol.*, vol. 1, no. 1, pp. 124–132, Sep. 2011.

[32] X. Y. He, C. Li, Z. H. Hu, and X. Guo, “Ultrahigh birefringent nonlinear silicon-core microfiber with two zero-dispersion wavelengths,” *J. Opt. Soc. Amer. B*, vol. 35, no. 1, pp. 122–126, 2018.

Tianyu Yang received the Bachelor’s and Master’s degrees in measurement and control technology from Hefei University of Technology, Hefei, China, in 2012 and 2016, respectively. He is currently working toward the Ph.D. degree in engineering at the University of Technology Sydney (UTS), Ultimo, NSW, Australia.

His current research interests include THz and optical photonic crystal fibers.

Q2 **Can Ding** (M’XX) received the bachelor’s degree in microelectronics from Xidian University, Xi’an, China, in 2009, and the Ph.D. degree from Macquarie University, Sydney, NSW, Australia, in 2015.

From 2012 to 2015, he was under the Cotutelle agreement between Macquarie University and Xidian University, China. During this period, he was also with Commonwealth Scientific and Industrial Research Organisation DPaS Flagship, Marsfield, Australia. From 2015 to 2017, he was a Postdoctoral Research Fellow with the University of Technology Sydney (UTS), Ultimo, NSW, Australia. He is currently a Lecturer with Global Big Data Technologies Centre, UTS. His research interests include the area of reconfigurable antenna, phase shifter, base station antenna, and THz waveguides.

Richard W. Ziolkowski (F’XX) received the B.Sc. (Hons.) (magna cum laude) degree in physics from Brown University, Providence, RI, USA, in 1974, the M.S. and Ph.D. degrees in physics from the University of Illinois at Urbana-Champaign, Urbana, IL, USA, in 1975 and 1980, respectively, and the Honorary Doctorate degree from the Technical University of Denmark, Kongens Lyngby, Denmark, in 2012. Q3

He is currently a Distinguished Professor with the University of Technology Sydney, Global Big Data Technologies Centre, Ultimo, NSW, Australia. He is also a Litton Industries John M. Leonis Distinguished Professor with the Department of Electrical and Computer Engineering and a Professor with the College of Optical Sciences, The University of Arizona, Tucson, AZ, USA. He was the Computational Electronics and Electromagnetics Thrust Area Leader with the Lawrence Livermore National Laboratory, Engineering Research Division, before joining The University of Arizona in 1990. He was the Australian DSTO Fulbright Distinguished Chair in Advanced Science and Technology from 2014 to 2015. He was a 2014 Thomas-Reuters Highly Cited Researcher. His current research interests include the application of new mathematical and numerical methods to linear and nonlinear problems dealing with the interaction of electromagnetic and acoustic waves with complex linear and nonlinear media, as well as metamaterials, metamaterial-inspired structures, and applications-specific configurations.

Dr. Ziolkowski is a Fellow of the Optical Society of America (OSA, 2006) and of the American Physical Society (APS, 2016). He served as the President of the IEEE Antennas and Propagation Society in 2005. He is also actively involved with the URSI, OSA, and SPIE professional societies.

Y. Jay Guo (F’14) received the Bachelor’s and Master’s degrees from Xidian University, Xi’an, China, in 1982 and 1984, respectively, and the Ph.D. degree from Xian Jiaotong University, Xian, in 1987. His research interests include antennas, mm-wave, and THz communications and sensing systems as well as big data. He has authored and coauthored more than 300 research papers and holds 22 patents in antennas and wireless systems. He is a Distinguished Professor and the founding Director of Global Big Data Technologies Centre at the University of Technology Sydney (UTS), Australia. Prior to this appointment in 2014, he served as a Director in CSIRO for over nine years, directing a number of ICT research portfolios. Before joining CSIRO, he held various senior leadership positions in Fujitsu, Siemens, and NEC in the U.K. He has chaired numerous international conferences.

Dr. Guo is a Fellow of the Australian Academy of Engineering and Technology, a Fellow of IET, and a member of the College of Experts of Australian Research Council. He was the recipient of a number of most prestigious Australian national awards, and was named one of the most influential engineers in Australia in 2014 and 2015. He was the International Advisory Committee Chair of IEEE VTC2017, General Chair of ISAP2015, iWAT2014 and WPMC’2014, and TPC Chair of 2010 IEEE WCNC, and 2012 and 2007 IEEE ISCIT. He served as the Guest Editor of special issues on “Antennas for Satellite Communications” and “Antennas and Propagation Aspects of 60-90GHz Wireless Communications,” both in IEEE TRANSACTIONS ON ANTENNAS AND PROPAGATION, Special Issue on “Communications Challenges and Dynamics for Unmanned Autonomous Vehicles,” IEEE JOURNAL ON SELECTED AREAS IN COMMUNICATIONS (JSAC), and Special Issue on “5G for Mission Critical Machine Communications,” IEEE NETWORK MAGAZINE.

GENERAL INSTRUCTIONS

- Authors: When accessing and uploading your corrections at the Author Gateway, please note we cannot accept new source files as corrections for your paper. Do not send new Latex, Word, or PDF files, as we cannot simply "overwrite" your paper. Please submit your corrections as an annotated PDF or as clearly written list of corrections, with location in paper, using line numbers provided on your proof. You can also upload revised graphics to the Gateway.
- Authors: Please note that once you click "approve with no changes," the proofing process is now complete and your paper will be sent for final publication and printing. Once your paper is posted on Xplore, it is considered final and the article of record. No further changes will be allowed at this point so please ensure scrutiny of your final proof.
- Authors: Unless invited or otherwise informed, overlength page charges of $260 per page are mandatory for each page in excess of seven printed pages and are required for publication. If you have any questions regarding overlength page charges, need an invoice, or have any other billing questions, please contact reprints@ieee.org as they handle these billing requests.

QUERIES

Q1. Author: Please verify that the funding information is correct.
Q2. Author: Please provide the year in which author became an IEEE Member.
Q3. Author: Please provide the year in which author became an IEEE Fellow.